

Large-eddy Simulations of Transverse Jet Mixing and Flame Stability in Supersonic Crossflow

ZHAO, Majie, YE, Taohong and LI, Qinling <<http://orcid.org/0000-0002-7191-9538>>

Available from Sheffield Hallam University Research Archive (SHURA) at:

<https://shura.shu.ac.uk/28086/>

This document is the Accepted Version [AM]

Citation:

ZHAO, Majie, YE, Taohong and LI, Qinling (2021). Large-eddy Simulations of Transverse Jet Mixing and Flame Stability in Supersonic Crossflow. AIAA Journal. [Article]

Copyright and re-use policy

See <http://shura.shu.ac.uk/information.html>

Large-eddy Simulations of Transverse Jet Combustion in Supersonic Cross-flow: Flame Stability and Mixing Mechanism

Majie Zhao* and Taohong Ye†

Department of Thermal Science and Energy Engineering, University of Science and Technology of China, Hefei, 230027, P.R. China

Qinling Li‡

Department of Engineering and Mathematics/MERI, Sheffield Hallam University, S1 1WB, United Kingdom

Large-eddy simulations (LES) combined with Partially Stirred Reactor (PaSR) combustion model are employed to investigate the turbulent mixing, combustion mode and flame stability of a sonic hydrogen jet injecting into high-enthalpy supersonic cross-flow at three momentum flux ratios J , i.e. 0.71, 2.11 and 4.00, respectively. The LES accuracy in terms of the turbulent kinetic energy, power spectra density and sub-grid Damköhler number is carefully addressed against various LES resolution criteria and the experimental mean pressure distribution on the upper wall. The ignition processes with auto-ignition and shock compression effects are identified and analyzed. At $J = 0.71$, the shock-induced ignition occurs behind the reflected shock wave and the combustion heat release is dominated by the premixed combustion. While for the high jet to cross-flow momentum flux ratios, e.g., $J = 2.11$ and 4.00, ignition happens toward around the jet orifice due to the strong bow shock and reflected shock effects and the combustion heat releases are dominated by the non-premixed combustion. Furthermore, the mechanisms of flame stabilization, local extinction and re-ignition in the transverse jet combustion in supersonic cross-flow are further analyzed with the chemical explosive mode analysis (CEMA).

* Ph.D. graduate, Department of Thermal Science and Energy Engineering, University of Science and Technology of China; zhaomj@mail.ustc.edu.cn.

† Associate Professor, Department of Thermal Science and Energy Engineering, University of Science and Technology of China; thye@ustc.edu.cn (Corresponding Author).

‡ Senior Lecturer, Department of Engineering and Mathematics/MERI, Sheffield Hallam University; q.li@shu.ac.uk.

Nomenclature

C_p	=	mixture specific heat at constant pressure, J/(kg·K)
D_m	=	diffusivity, m ² /s
D	=	diameter of jet orifice, m
Da	=	Damköhler number
e	=	internal energy, J/kg
E	=	total energy, J/kg
h_s	=	sensible enthalpy, J/kg
L	=	axial length of computational, m
Ma	=	Mach number
N	=	Number of points
P	=	static pressure, Pa
Pr	=	Prandtl number
r	=	distance from the center of jet orifice, m
r_0	=	jet radius, m
R	=	mixture gas constant, J/(kg · K)
Re	=	Reynolds number
Sc	=	Schmidt number
T	=	gas temperature, K
H	=	enthalpy flux
J	=	jet to cross-flow flux ratio
k	=	turbulent kinetic energy, J
u	=	gas velocity, m/s
U	=	mean velocity of cross-flow, m/s
U_j	=	mean velocity at the center of the injection orifice, m/s
Y	=	mass fraction
y^+	=	dimensionless wall distance
x, y, z	=	spatial coordinate

$\dot{\omega}$	=	source terms
μ	=	dynamic viscosity, kg/(m · s)
ν	=	kinematic viscosity, kg/(m · s)
v'	=	sub-grid velocity fluctuation, m/s
ε	=	dissipation rate of turbulent kinetic energy, m ² /s ³
Δ	=	LES filter, m
λ	=	molecular thermal diffusivity, m ² /s
θ_0	=	initial momentum thickness, m
τ_c	=	chemical reaction time, s
τ_*	=	sub-grid turbulent mixing time, s
τ_Δ	=	sub-grid time scale, s
τ_k	=	Kolmogorov time scale, s
δ_l	=	laminar flame thickness, m
s_l	=	laminar flame speed, m/s
ρ	=	density, kg/m ³

Subscripts

sgs	=	quantity related to sub-grid scale
t	=	turbulent
i, j	=	Cartesian components of a vector
m	=	index for species
T	=	temperature
RES	=	resolved
HRR	=	heat release rate
x, y, z	=	spatial coordinate
F	=	fuel
O	=	oxidant

Superscripts

sgs	=	quantity related to sub-grid scale
-------	---	------------------------------------

I. Introduction

Transverse jet in supersonic cross-flow (JISCF) is one of the most fundamental flow phenomena in supersonic combustion chambers [1–5], such as the actual flight vehicle Hyshot II [6,7] and the supersonic combustion experiments by Gamba et al. [8,9]. In JISCF combustion chambers, there exist complex shock train, flame, turbulence and boundary layer interactions [6–15]. In addition to auto-ignition due to high-enthalpy and shock aerodynamic heating, local extinction caused by turbulent small-scale vortex and re-ignition, there is also strong coupling between the density, pressure, temperature and velocity. The change in density is not only due to the exothermic heat release of the combustion chemical reaction, but also the viscous compression of the supersonic flows. Therefore, the JISCF combustion is a great challenge, and fundamental understanding about the mixing, combustion and flame stabilization at supersonic regime is still limited [16,17].

The main shock waves and flow structures of a sonic jet in supersonic crossflow [10] are illustrated in Figure 1. The bow shock wave and the recirculation zone upstream of the jet orifice contribute to auto-ignition and flame anchoring for higher jet to cross-flow flux ratio [10,18], which is defined as $J = \rho_j U_j^2 / \rho_\infty U_\infty^2$. The distributed reaction zone along the horseshoe vortex region is also observed for the higher jet to crossflow flux ratios [10]. However, for lower jet to cross-flow flux ratio, the flame cannot be anchored in the upstream recirculation zone of the jet orifice and the region after the relatively weak bow shock due to low temperature after the bow shock. In the meantime, the flame appears to be lifted up and stabilized within the wake of wall boundary layer downstream of the jet orifice [10]. LES studies of the HyShot II combustor by Fureby et al. [19,20] showed that auto-ignition of longitudinal oscillation was observed between 30D and 60D downstream of fuel jet orifice due to the intermittent “hot spot” phenomenon. The flame structure is very different from that in the low-speed combustors [17]. The results of Ben-Yakar [18] suggested that auto-ignition firstly appeared in the recirculation zone upstream the hydrogen jet and the flame extended along the outer boundary of the jet plume, while local extinction phenomenon was observed at the interface between the fuel jet plume and supersonic cross-flow just downstream of the jet orifice. Gamba et al. [8,21] studied supersonic transverse jet combustion with a compression ramp at the combustor inlet to generate a shock train in the combustor chamber. The shock train interacts with the hydrogen jet mixing layer by shock compression and heating, which provides a mechanism of flame stabilization. Experimental study of Mai et al. [11] demonstrated that the existence of an oblique shock in supersonic transverse

jet combustion can increase the reaction area and the recirculation zone downstream of fuel jet orifice, which increased the flow residence time, and thus contributed to the flame stabilization.

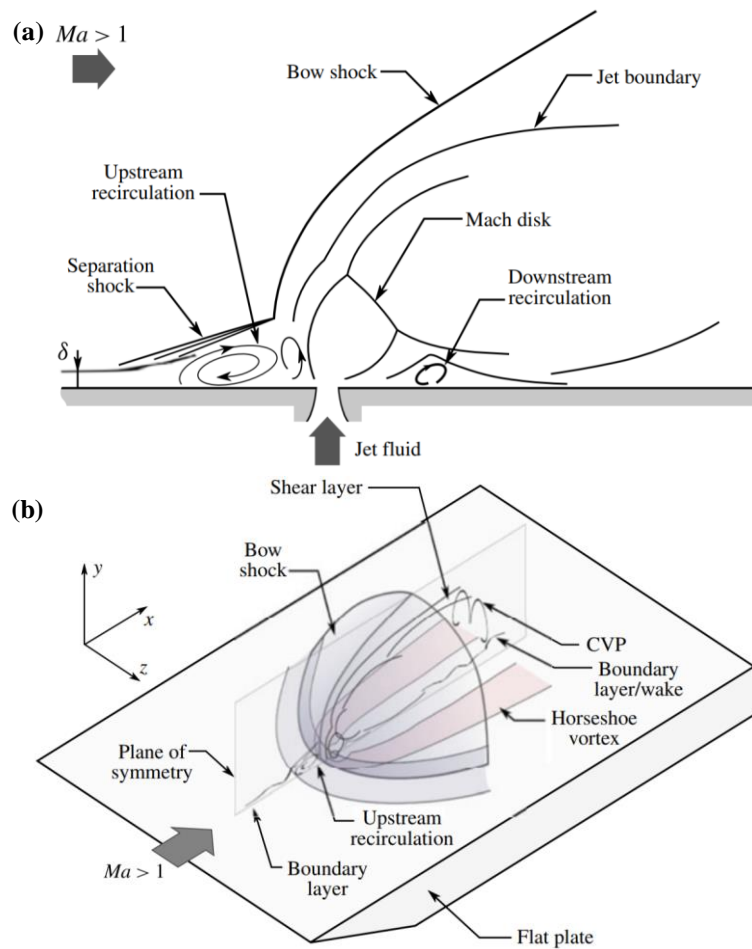


Fig. 1 Schematic diagrams of a transverse jet in supersonic crossflow: (a) side-view; (b) three-dimensional view of the flow field features [10].

Luo et al. [22] analyzed the direct numerical simulation (DNS) results of supersonic jet combustion using the Takeno flame index (TFI) combined with the heat release rate, indicating that there were both premixed and non-premixed combustions in the supersonic jet combustion. The CEMA was used by Fureby et al. [23] to study supersonic combustions in a strut injector, suggesting that combustion in two-stage injection struts consists of auto-ignition zones enfolded by auto-igniting fronts embedded in a background of non-premixed flames. Moule et al. [24] used LES combined with Partially Stirred Reactor (PaSR) combustion model to study supersonic jet combustion where the flame was found to anchor at the beginning of a shock diamond. The very large pressure gradient and heat release rate in the flame stabilization region indicate that there is a strong coupling between shock compression and combustion. Although it is thought the mixing process mainly dominates the supersonic combustion process [2,3], several numerical studies [22,24–28] suggest that there exists partially premixed flame in the supersonic combustion systems. There are more evidences from experimental and numerical studies that

the flame mechanism in supersonic combustion is mainly distributed reaction zone and thin reaction zone [9,10,29,30]. In the supersonic transverse jet combustion, the flame near the wall is a distributed reaction zone regime, while the combustion in the shear layer is a thin non-premixed reaction layer [10]. Moreover, the interaction between various scale turbulence structures in the distributed reaction zone regime make the combustion flame mode much more complex [31].

However, the fundamental understanding of JISCF combustion about the mixing, combustion and flame at supersonic regime is very limited [16,17], which motivate the current work. The experiments of supersonic transverse jet combustion by Stanford University [8,21] have been numerically studied by some researchers [14,27,32–34], but most of them are mainly concerned with testing the turbulent compressible combustion models, whereas details of the flame stability and mixing mechanism with different jet to cross-flow flux ratios are not enough. Based on experiments of the supersonic transverse jet combustion [8,21], LES combined with PaSR combustion model is used to study turbulent mixing and combustion processes of transverse sonic jet in supersonic cross-flow at three jet to cross-flow flux ratios. The PaSR model estimates the filtered reaction rate directly with the filtered quantities, thereby neglecting the interactions between combustion and turbulence at the sub-grid scale. When a fine mesh is used to ensure the sub-grid scale Damkohler number (Da_{sgs}) less than unity [35][24][36], the multiple physics of high-speed combustion, such as auto-ignition and shock / flame interactions, can be captured by using the PaSR model. The CEMA method proposed by Lu et al. [37] is utilized to identify typical combustion modes in the combustor. In addition, due to the existence of the shock train generated in the scramjet engine combustion chamber, the interaction between the jet flame and the shock waves are investigated to deepen the understanding of the flame stabilization mechanism and the complicated mixing and combustion processes. The rest of the paper is organized as follows: in Section 2, physical model and numerical method are presented. The numerical results are presented and discussed in Section 3. Finally, the main conclusions drawn from our work are summarized in Section 4.

II. Physical Model and Numerical Methods

A. Physical model

Figure 2 shows the schematic of the high-enthalpy hydrogen JISCF combustor, similar to the experimental setup at Stanford University [8,21]. The supersonic oncoming freestream air, with Mach number of 2.8, has a high static temperature of $T_a = 1200$ K. The perpendicular wall sonic fuel jet enters the supersonic stream and interacts with the high-enthalpy supersonic cross-flow. The injection orifice with a diameter of $D = 2$ mm is located at 70

mm downstream the cross-flow inlet. The inlet height of the combustor is 23 mm. The compression ramp has a convergence angle of 10° to generate a shock train. The height of constant area section is 15 mm in the y-direction with a span of 75 mm in the z-direction. The jet to cross-flow momentum ratio, J , is equal to 0.71, 2.11 and 4.0, respectively, to investigate the supersonic transverse hydrogen jet combustion process in the present study. The detailed flow conditions of the oncoming air stream and the hydrogen jet are given in Table 1.

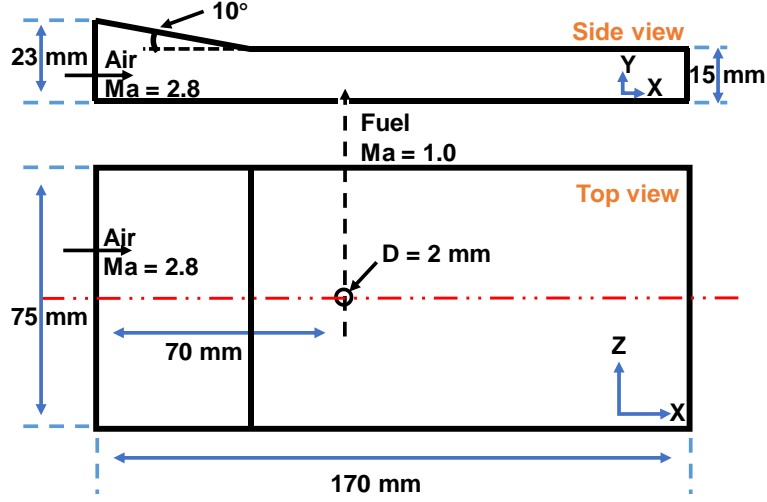


Fig. 2 Schematic of the JISCF combustor.

Table 1 Inflow conditions of the hydrogen jet and the air stream.

Case	Ma	P/kP_a	T/K	$Y(H_2)$	$Y(O_2)$	$Y(N_2)$
$J = 0.71$	1.0	225	250	1.0	0	0
$J = 2.11$	1.0	668.25	250	1.0	0	0
$J = 4.00$	1.0	1286.3	250	1.0	0	0
Air	2.8	40	1200	0	0.232	0.768

B. Numerical methods

The filtered LES compressible governing equations are

$$\frac{\partial \bar{\rho}}{\partial t} + \frac{\partial \bar{\rho} \tilde{u}_j}{\partial x_j} = 0, \quad (1)$$

$$\frac{\partial \bar{\rho} \tilde{u}_i}{\partial t} + \frac{\partial \bar{\rho} \tilde{u}_i \tilde{u}_j}{\partial x_j} = -\frac{\partial \bar{p}}{\partial x_i} + \frac{\partial}{\partial x_j} (\bar{\tau}_{ij} - \tau_{ij}^{sgs}), \quad (2)$$

$$\frac{\partial \bar{\rho} \tilde{E}}{\partial t} + \frac{\partial}{\partial x_j} [(\bar{\rho} \tilde{E} + \bar{p}) \tilde{u}_j] = \frac{\partial}{\partial x_j} \left[\lambda \frac{\partial \tilde{T}}{\partial x_j} + \tilde{u}_i \bar{\tau}_{ij} - H^{sgs} - \sigma^{sgs} \right] + \bar{\omega}_T, \quad (3)$$

$$\frac{\partial \bar{\rho} \tilde{Y}_m}{\partial t} + \frac{\partial \bar{\rho} \tilde{u}_j \tilde{Y}_m}{\partial x_j} = \frac{\partial}{\partial x_j} \left[\bar{\rho} D_m \frac{\partial \tilde{Y}_m}{\partial x_j} - \tau_{\tilde{\phi}}^{sgs} \right] + \bar{\omega}_m \quad (m = 1, \dots, N), \quad (4)$$

$$\bar{P} = \bar{\rho}R(\bar{Y}_m)\bar{T}, \quad (5)$$

where, $\bar{\rho}$, \tilde{u}_j , \bar{Y}_m , \bar{p} and \bar{T} are filtered density, velocity, mass fraction of species m , pressure and temperature, respectively. D_m in equation (4) is the molecular mass diffusivity, and is calculated through $D_m = \lambda/\rho C_p$ with unity Lewis number assumption. λ is the molecular thermal conductivity, and estimated using the Eucken approximation [38], $\lambda = \mu C_v(1.32 + 1.37 \cdot R(\bar{Y}_m)/C_v)$, where $\mu = \frac{A_s\sqrt{T}}{1+\frac{T_s}{T}}$ is the dynamic viscosity by using Sutherland's law. Here $A_s = 1.67212 \times 10^{-6} \text{ kg/m} \cdot \text{s} \cdot \sqrt{\text{K}}$ is the Sutherland coefficient, while $T_s = 170.672 \text{ K}$ is the Sutherland temperature. C_v is the heat capacity at constant volume and derived from $C_v = C_p - R(\bar{Y}_m)$. Here $C_p = \sum_{m=1}^M \bar{Y}_m C_{p,m}$ is the heat capacity at constant pressure, and $C_{p,m}$ is estimated from JANAF polynomials [39]. $R(\bar{Y}_m)$ is specific gas constant and is calculated from $R(\bar{Y}_m) = R_u \sum_{m=1}^M Y_m MW_m^{-1}$. MW_m is the molar weight of m -th species and R_u is universal gas constant. The filtered viscous stress $\bar{\tau}_{ij}$ is defined based on the Eddy viscosity hypothesis as

$$\bar{\tau}_{ij} = \mu \left(2\bar{S}_{ij} - \frac{2}{3}\mu\bar{\zeta}_{kk}\delta_{ij} \right), \quad (6)$$

where, $S_{ij} = \frac{1}{2} \left(\frac{\partial u_j}{\partial x_i} + \frac{\partial u_i}{\partial x_j} \right)$ is the strain rate tensor and δ_{ij} is the kronecker operator. The filtered total energy is

$$\bar{E} = \bar{e} + \frac{1}{2}\bar{u}_j^2 + k^{sgs}, \quad (7)$$

where, $\bar{e} = \bar{h}_s - \bar{P}/\bar{\rho}$ is internal energy, $\frac{1}{2}\bar{u}_j^2$ is resolved kinetic energy and k^{sgs} is the sub-grid kinetic energy.

The \bar{h}_s in the equation of internal energy is sensible enthalpy, expressed as

$$\bar{h}_s = \sum_{m=1}^N \bar{Y}_m \int_{T_0}^{\bar{T}} C_{p,m} dT, \quad (8)$$

The reaction source term in the filtered energy equation (4) is

$$\bar{\dot{\omega}}_T = \sum_{m=1}^N \bar{\dot{\omega}}_m \Delta h_{f,m}^o. \quad (9)$$

All the sub-grid scale terms, denoted by superscript ‘‘sgs’’ in the governing equations (1) - (4), are closed by the Wall-Adapting Local Eddy-viscosity (WALE) model [40,41]. The sub-grid enthalpy flux H^{sgs} and the sub-grid viscous work σ^{sgs} in Eqs. (3) are closed as

$$H^{sgs} + \sigma^{sgs} = -\frac{\mu_t C_p}{Pr_t} \frac{\partial \bar{T}}{\partial x_j} - (\mu_t + \mu) \frac{\partial k^{sgs}}{\partial x_j} + \tilde{u}_i \bar{\tau}_{ij}^{sgs}, \quad (10)$$

where the sub-grid kinetic energy and viscosity are modelled by $k^{sgs} = (C_w^2 \Delta^2 / C_k)^2 (\overline{OP})^2$ and $\mu_t = (C_w \Delta)^2 \overline{OP}$, in which C_k and C_w are constants and take the values of 0.094 and 0.325 respectively [40]. $\Delta = \sqrt[3]{\Delta_x \Delta_y \Delta_z}$ is the

filter width, $\overline{OP} = \frac{(S_{ij}^d S_{ij}^d)^{3/2}}{(\tilde{s}_{ij} \tilde{s}_{ij})^{5/2} + (S_{ij}^d S_{ij}^d)^{5/4}}$ and $S_{ij}^d = \tilde{S}_{ik} \tilde{S}_{kj} + \tilde{\Omega}_{ik} \tilde{\Omega}_{kj} - \frac{1}{3} \delta_{ij} [\tilde{S}_{mn} \tilde{S}_{mn} + \tilde{\Omega}_{mn} \tilde{\Omega}_{mn}]$, in which $\tilde{\Omega}_{ij}$ is

the anti-symmetric part of $\nabla \tilde{u}$. And $\tau_{ij}^{sgs} = \mu_t (2\tilde{S}_{ij} - \frac{2}{3} \delta_{ij} \tilde{S}_{kk})$. The turbulent Prandtl number is set as $Pr_t = 0.9$ [42]. The sub-grid scalar stresses are approximated using an eddy-diffusivity model, which is written as,

$$\tau_{\tilde{Y}_m}^{sgs} = \bar{\rho} (\widetilde{u_i \tilde{Y}_m} - \tilde{u}_i \tilde{Y}_m) = -\bar{\rho} \tilde{D}_t \nabla \tilde{Y}_m, \quad (11)$$

where \tilde{D}_t is the turbulent diffusivity modeled as $\bar{\rho} \tilde{D}_t = \mu_t / Sc_t$. The turbulent Schmidt number is set as $Sc_t = 0.7$ [42].

The Partially Stirred Reactor (PaSR) model [43][44] is used to model the supersonic turbulent combustion, which has been successfully applied to the simulations of turbulent combustion in scramjet engines [19,20,45,46]. In the PaSR model, it is assumed that the reacting flow is composed of reacting fine structures and the surroundings dominated by the large scale structures [43]. The ratio of the fine reacting structures volume to the LES cell volume κ is modelled as [43]

$$\kappa = \frac{\tau_c}{\tau_c + \tau_*}, \quad (12)$$

where, $\tau_c = \delta_l / s_l \approx \nu / s_l^2$ and $\tau_* = \sqrt{\tau_\Delta \tau_k}$ denote the chemical reaction time and subgrid turbulent mixing time, respectively. Here, δ_l is the laminar flame thickness and s_l is the laminar flame speed. $\tau_\Delta = \Delta / \nu'$ is the sub-grid time scale and $\tau_k = (\nu / \varepsilon)^{1/2}$ is the Kolmogorov time scale, where $\nu' = \sqrt{2k^{sgs}/3}$ is the sub-grid velocity fluctuation, ν is the laminar kinematic viscosity and $\varepsilon = \nu'^3 / \Delta$ is the sub-grid dissipation rate. It should be noted that there are many available options to estimate the chemical time scale, and here we follow the recent computational investigation performed with the same formulation [24][43]. Moreover, as in Refs. [24][43], the filtered reaction rate $\bar{\omega}_m$ can be approximated as $\bar{\omega}_m \approx \kappa \bar{\omega}_m^*$, where $\bar{\omega}_m^*$ is the quasi-laminar chemistry reaction rate based on the filtered variables. It can be seen that this time scale is only to obtain an approximate value for the fine structure volume fraction κ . Based on the formulation of κ , one can see that if the mesh is fine enough, the PaSR model can be seen as a quasi-laminar chemistry model with sufficiently small subgrid turbulent mixing time, i.e. $\kappa \rightarrow 1$.

A chemical kinetics model [47] of 9 species (H_2 , H , O_2 , O , OH , HO_2 , H_2O_2 , H_2O & N_2) and 19 reaction steps for hydrogen/air combustion is adopted to describe the combustion process. The mechanism is validated by comparing the laminar flame speed, ignition delay time and extinction strain rate with previous experimental data [48–50]. Good agreement has been achieved as seen in Fig. 3. Besides, this mechanism has also been validated in the previous work on rotating detonation simulations [51] and used in other previous investigations for supersonic combustion [24,44].

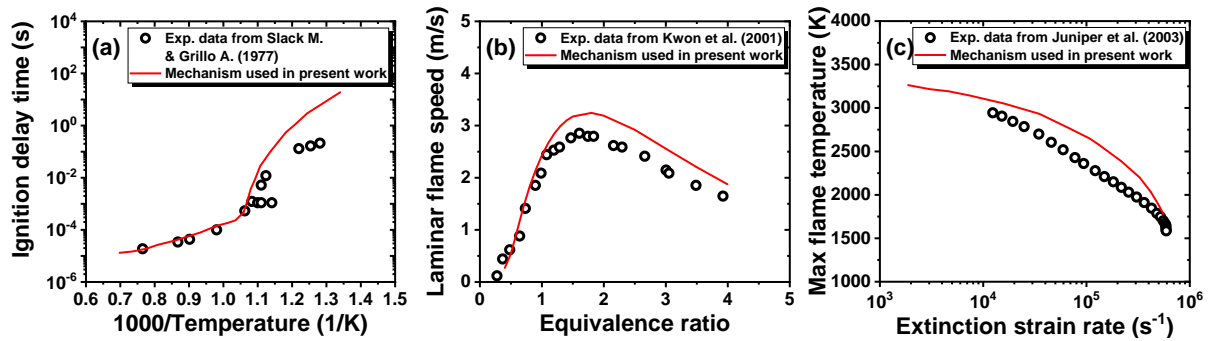


Fig. 3 Comparison of (a) ignition delay time, (b) laminar flame speed and (c) extinction strain rate from present H₂-air mechanism with previous experimental data [48–50].

The governing equations, i.e. Eqs. (1) – (4), are discretized with cell-centered finite volume method and solved by a density-based solver, which is developed from the fully compressible non-reactive flow solver *rhoCentralFoam* in the framework of OpenFOAM [52]. The convective fluxes are reconstructed using a second order (flux limiter-based) TVD scheme and the viscous diffusion fluxes are implemented using the second order central differencing scheme. An explicit modified fourth order Runge-Kutta scheme with low storage requirement [53] is used for time integration. The marching time-step is adjusted according to Courant number under 0.25 to capture the unsteady flow field structure. The solver has also been validated in our previous simulations of sonic injection from circular injector into a supersonic cross-flow [54,55]. In addition, for each case, the time-averaging is performed with six flow through times ($6L/U$), before which each case is run for four flow through times ($4L/U$) to ensure the statistical convergence, where L is the axial length of computational domain and U is the mean velocity of cross-flow.

Three sets of computational mesh, the coarse, middle and fine, with 4.8, 26.52 and 85 million cells, respectively, are used for the mesh sensitivity analysis. Figure 4 shows the schematic of the grid in the central plane and normal y -direction plane. Hexahedral meshes are utilized with O-type employed for the fuel injection. In order to improve numerical accuracies, mesh refinement is performed near the wall and the injection orifice to

yield $y^+ \leq 1$ for the first grid adjacent to the wall for the fine mesh. More detailed information of the mesh can be seen in table 2.

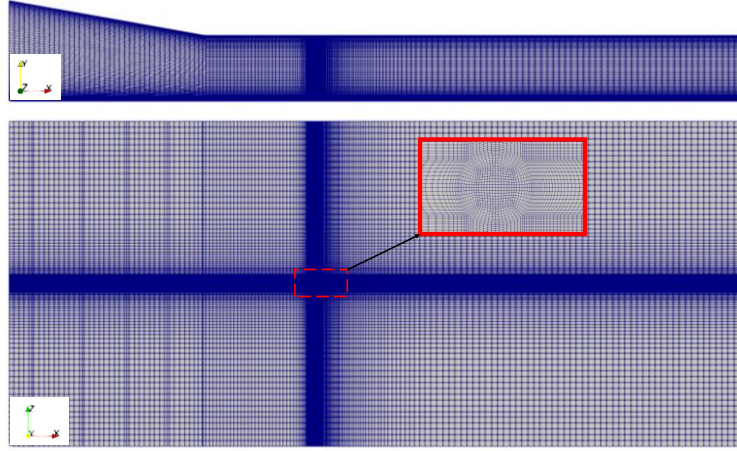


Fig. 4 Schematic of the grid on the central plane and normal y-direction plane.

Table 2 Detailed information of mesh.

Mesh	$N_x \times N_y \times N_z$	Total number	y^+ of up wall	y^+ of down wall
Coarse mesh	401×61×201	4.8 million	2.4 ~ 4.3	1.3 ~ 3.7
Middle mesh	651×121×341	26.52 million	0.8 ~ 2.1	0.5 ~ 1.4
Fine mesh	1001×171×501	85 million	≤ 1	≤ 1

The supersonic crossflow and sonic jet boundary conditions are set as fixed value based on the parameters provided in Table 1. The supersonic crossflow and jet inlet are specified with the first type of boundary condition. Due to the high-speed flow through the combustion chamber, an adiabatic no-slip wall boundary condition is employed at walls. For the outlet boundary, a non-reflection condition is utilized to avoid spurious wave reflections from the outlet boundary towards the upstream region, in which the boundary value is determined by solving the equation of $\frac{D\phi}{Dt} = \frac{\partial\phi}{\partial t} + \mathbf{u} \cdot \nabla\phi = 0$, where ϕ is the boundary value and \mathbf{u} is the velocity vector. A periodic boundary condition is applied in the span-wise boundaries. The crossflow inlet mean velocity profile is taken from an additional three-dimensional RANS simulation [56,57]. The turbulence perturbation is specified using white noise with 5% intensity for all cases since the turbulence flow statistics are not measured in the experiments [21]. Note that the crossflow inlet is located at 35D upstream of the fuel jet, which means that the turbulent random velocity fluctuations added would have little effects on the flame behaviours with such a long distance. The fuel jet inlet mean velocity profile is prescribed by a hyperbolic-tangent function [57],

$$\frac{\tilde{u}}{U_j} = \frac{1}{2} \left\{ 1 - \tanh \left[\frac{1}{4\theta_0} \left(\frac{r}{r_0} - \frac{r_0}{r} \right) \right] \right\}, \quad (13)$$

where, U_j is the mean velocity at the center of the injection orifice, $r = \sqrt{y^2 + z^2}$, r_0 is the jet radius, and the initial momentum thickness θ_0 is 0.045D [58].

C. Numerical validation

According to the work of Pope [59], at least 80% of the total turbulent kinetic energy (TKE) being resolved indicates a well-resolved LES. The well-established resolution criterion is defined as,

$$Me = \frac{k_{sgs}}{k_{RES} + k_{sgs}}, \quad (14)$$

where k_{sgs} is the sub-grid turbulent kinetic energy and k_{RES} is the resolved turbulent kinetic energy,

$$k_{RES} = \frac{1}{2} \langle \langle \tilde{u}_i^2 \rangle - \langle \tilde{u}_i \rangle^2 \rangle, \quad (15)$$

where $\langle \cdot \rangle$ represents an ensemble averaging. Fig. 5 shows the distributions of Me with different mesh, which is computed using the data where hydrogen exists ($Y_{H_2} > 0.001$) for the fine mesh. It is shown that the probability density distributions of grids with the well-established turbulence resolution criterion, i.e. $Me < 0.2$, are about 0.97, 0.88 and 0.70 for fine, middle and coarse mesh respectively. Although most grids of the middle mesh meet the well-established turbulence resolution criterion, there are still considerable grids (about 12%) that do not meet the well-established turbulence resolution criterion. Therefore, the results with fine mesh is used in the section of results and discussion.

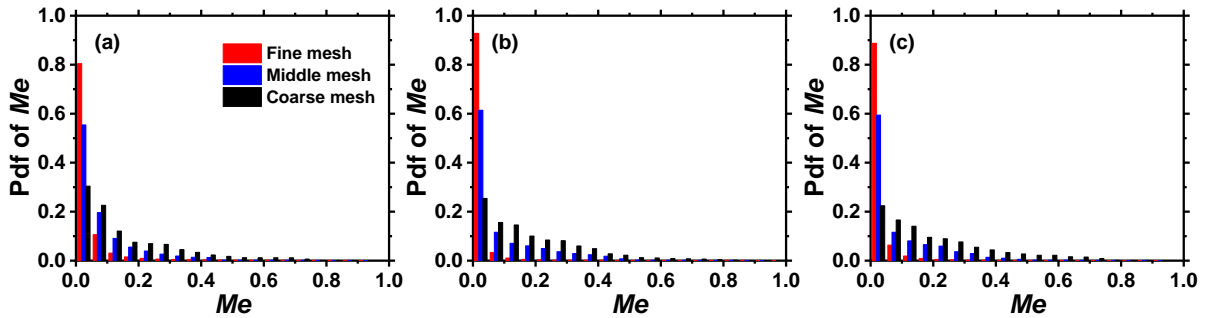


Fig. 5 Probability Density Distributions of Me with different mesh, (a) $J = 0.71$, (b) $J = 2.11$ and (c) $J = 4.00$.

The power spectra density (PSD) provides the turbulence energy spectra, which is widely used to evaluate the quality of an LES result [60–62]. Figure 6 shows the PSD of the pressure in the shear layers for each case with fine mesh. Moreover, PSD of the streamwise velocity (velocity in the x-direction) in the shear layer for each case is shown in Fig. 7. The PSD results in Figs. 6 and 7 yield good agreement with the $-5/3$ law also indicating that

the effective LES filtering does occur in the inertial subrange region [59]. Therefore, the current LES solver and mesh quality are capable to predict the characteristic of large and small resolved structures.

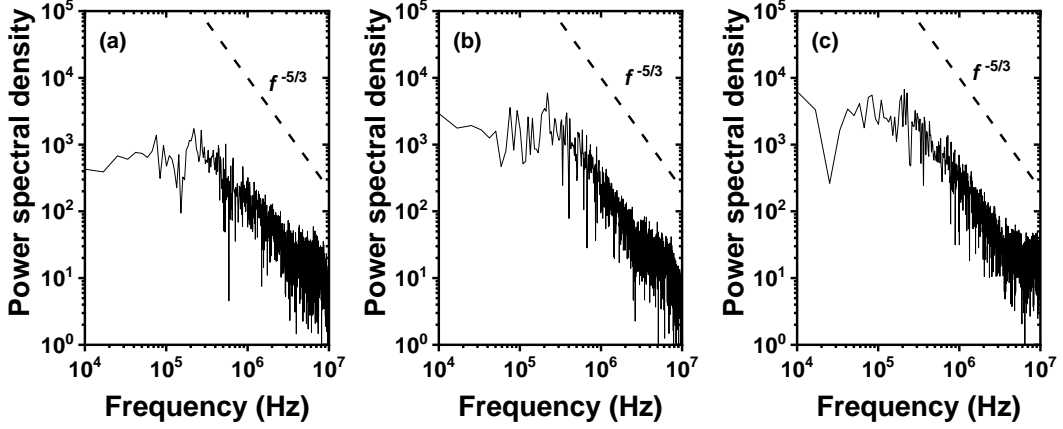


Fig. 6 PSD of pressure in the shear layer, (a) $J = 0.71$, (b) $J = 2.11$ and (c) $J = 4.00$.

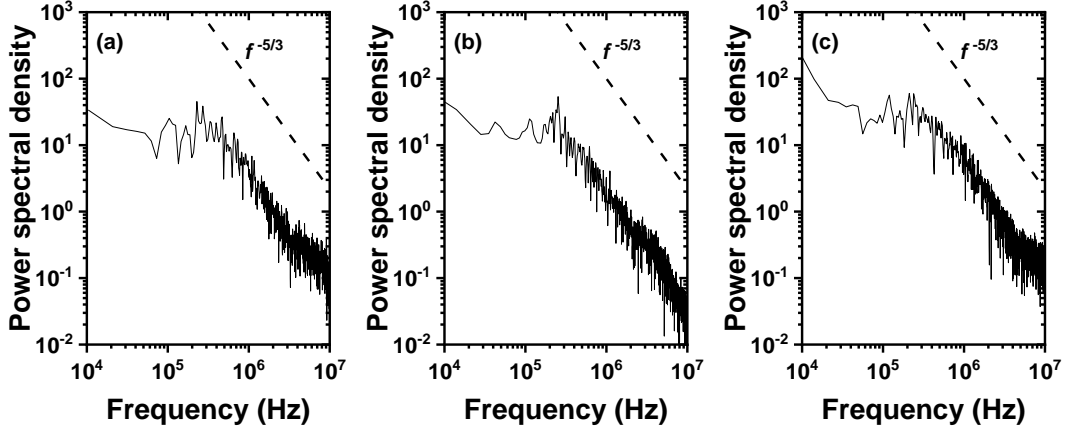


Fig. 7 PSD of the streamwise velocity (velocity in the x-direction) in the shear layer for each case with fine mesh, (a) $J = 0.71$, (b) $J = 2.11$ and (c) $J = 4.00$.

On the other hand, the sub-grid Damköhler numbers (Da_{sgs}) proposed by Krol et al. [63] are used to assess the effect of sub-grid fluctuations on the filtered chemical reaction source terms, which is defined as

$$Da_{sgs} = \frac{\tau_{sgs}}{\tau_c}, \quad (16)$$

where, τ_{sgs} is the characteristic time of the smallest resolved structure, determined with

$$\tau_{sgs} = \sqrt{\frac{\nu_t}{\varepsilon_{sgs}}}, \quad (17)$$

where, ν_t is sub-grid turbulent viscosity and ε_{sgs} is the sub-grid dissipation. τ_c is the characteristic time of the chemistry, which is evaluated as $\tau_c = \delta_l/s_l \approx \nu/s_l^2$ [43]. Note that although there are many options available for

the chemical time scale, it is not easy to estimate the chemical time scale for a relatively complex combustion system including non-premixed or partially premixed combustion and as an estimation, here it is assumed based on the laminar flame thickness and the laminar flame speed only for the sake of simplicity. If the sub-grid Damköhler numbers are much less than 1, the time scale of the chemical reaction is fully solved and the impact of sub-grid fluctuations on the filtered chemical reaction source terms can be ignored [35,64]. Fig. 8 illustrates the probability density distributions (pdf) of the sub-grid Damköhler number where the instantaneous heat release rate is greater than one-thousandth of the maximum heat release rate for each case with different mesh, i.e. fine, middle and coarse mesh. It is clear to see that the sub-grid Damköhler numbers of the region where the combustion exists are always less than 0.3, with most regions being less than 0.1 for the fine mesh, which suggests that the effect of sub-grid fluctuations on the filtered chemical source term can be ignored [35,64]. However, for the results of middle and coarse meshes, there would be some effects of sub-grid fluctuations on the filtered chemical reaction source term, which may affect the analysis of flame dynamics.

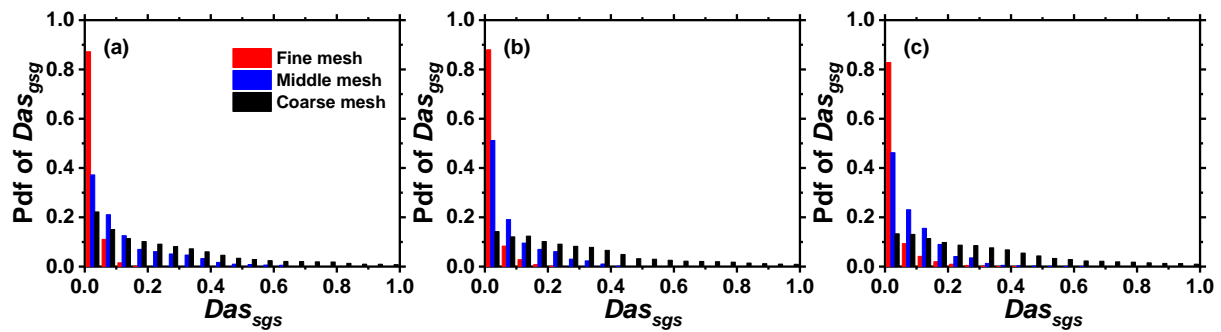


Fig. 8 Probability Density Distributions of the sub-grid Damköhler numbers (Da_{sgs}) with different mesh, (a) $J = 0.71$, (b) $J = 2.11$ and (c) $J = 4.00$.

Furthermore, Figure 9 shows the current predicted and experimental results of mean pressure distributions on the upper wall of the combustor. The LES results show a fairly good agreement with the experiments of Gamba et al. [8,21]. The results of different grids show a reasonable mesh convergence. Note that the differences between the simulations and experiment at $x/D > 35$ for $J = 4$ are observed, which may be due to that some extra heat transfer such as radiation on the wall is not included in the simulations. The well resolved 80% total turbulent kinetic energy, the PSD following a slope of $-5/3$, the small sub-grid Damköhler numbers, and the mean pressure distribution indicate that the current numerical simulation methods and fine mesh are able to provide the reliability basis for the next LES analysis.

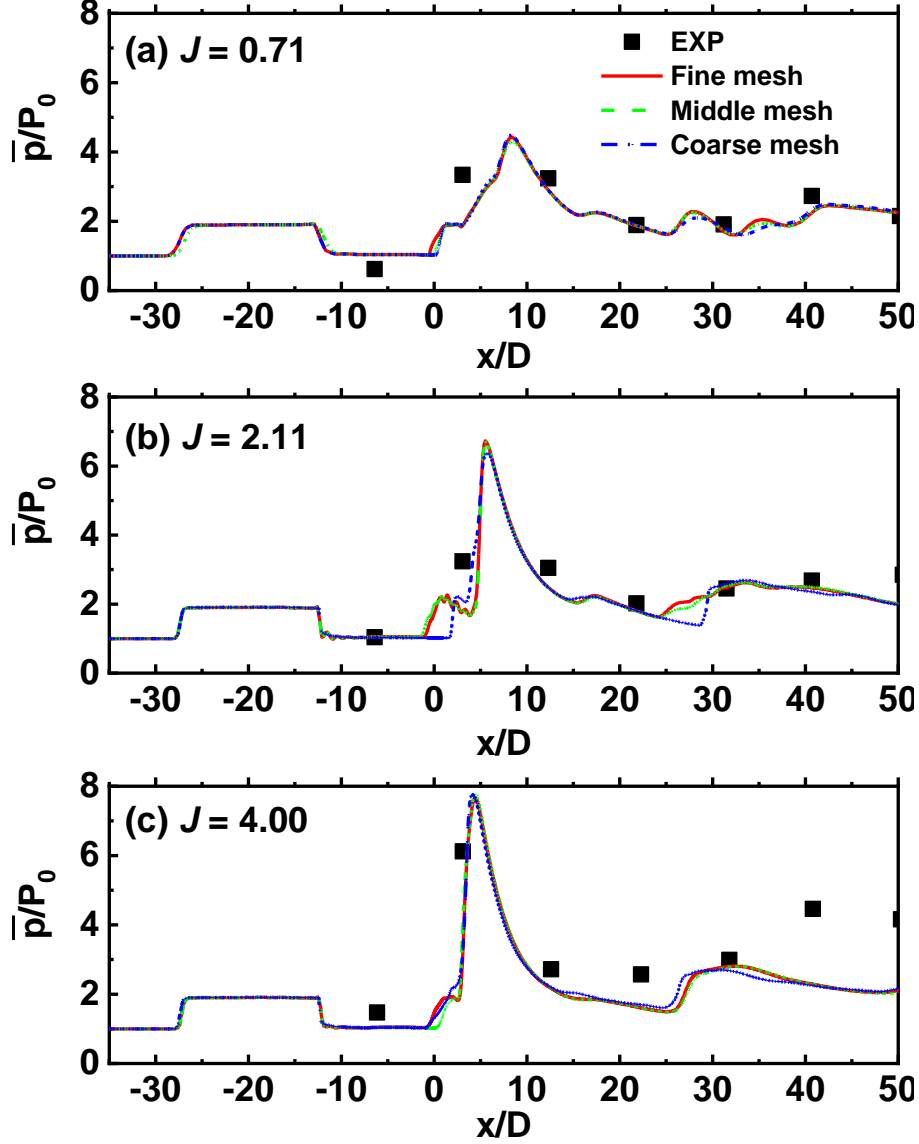


Fig. 9 Comparison of mean pressure distribution on the upper wall between present simulation and experiments of Gamba et al. [8,21] on the central plane, $J = 0.71$ 、 2.11 and 4.00 , respectively.

III. Results and Discussions

A. Flame structures and shock waves

Figure 10 predicts the instantaneous distributions of OH mass fraction and OH-PLIF snapshot by Gamba et al. [8,21] in the central plane ($z/D = 0$). Both experiments and the current results prove that the distance between the upper and lower flame OH mass fraction increases with the momentum flux ratio, J . For the lower jet to cross flux ratio $J = 0.71$, there is no obvious flame in the region of $x/D < 14$ in the experiment [8] and the current study. The interaction between the reflecting oblique shock wave from the upper wall and the jet mixing layer increases the local temperature, forms the flame from $x/D = 14$. However, the current predicted flame appears further downstream compared with the experiment, which may be due to the fact that the reflected shock wave propagates

upstream in the experiment over time [8] or slightly different inlet boundary condition employed in the LES study. Moreover, the predicted flame is slightly stronger in the near wall region for $J = 2.11$ and 4.00 , which may be due to the slightly different boundary condition with the experiments. Here only one predicted instantaneous structure is shown here and the overall predicted OH and experimental OH-PLIF snapshot have similar flame characteristics, such as local extinction, shock enhanced combustion of flames, even the similar trend of increasing shear layer distance with J . Moreover, the OH* chemiluminescence image of $J = 2.11$ has been measured in the experiment by Gamba et al. [8], and the qualitative comparison between experimental result and the time-averaged distribution of OH mass fraction in the central plane ($z/D = 0$) for $J = 2.11$ is shown in Fig. 11. The results suggest that some phenomena observed in the experiment, such as the flame in the upstream recirculation zone of jet orifice, enhanced flame behind the bow shock and reflected oblique shock waves, thin reaction zones and local flame extinction or quenching in the windward jet shear layer, are also captured by the present LES simulations.

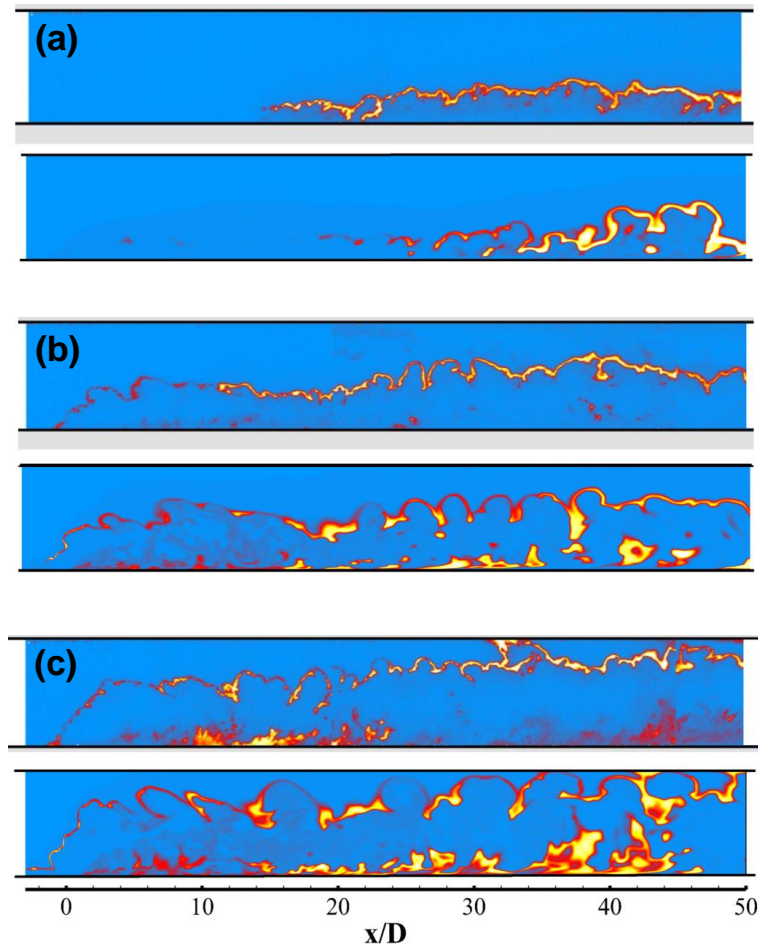


Fig. 10 OH-PLIF snapshot by Gamba et al. [8] (top) and the predicted results of instantaneous distribution of OH mass fraction (down) on the central plane ($z/D = 0$) for (a) $J = 0.71$, (b) $J = 2.11$ and (c) $J = 4.00$, respectively.

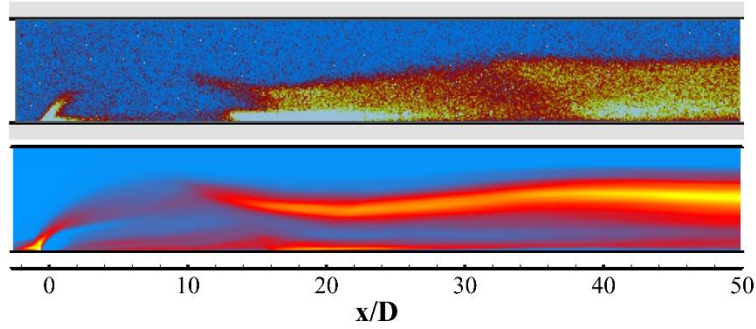


Fig. 11 OH* chemiluminescence image by Gamba et al. [8] (top) and the predicted results of mean distribution of OH mass fraction (down) on the central plane ($z/D = 0$) for $J = 2.11$.

In addition, the contours of heat release rate and pressure (represented by the solid lines range from 20KPa to 800Kpa) in the central plane ($z/D = 0$) are shown in Fig. 12. A second shock- train, formed by the bow and lambda shocks around the hydrogen jet orifice, combines with the combustor inlet shock-train to generate a complex three-dimensional shock-pattern along the combustor. From Fig. 12(a), it can be seen clearly that ignition of the jet mixing layer appears just after the reflected shock wave. For the higher jet to cross flux ratios $J = 2.11$ and 4.00, the flames can be anchored in the recirculation zone upstream of the jet orifice (see Figs. 10b and 10c) due to the compression heating by the relatively strong bow shock. The windward-side flames are wrinkled and stretched caused by the unstable characteristics of jet shear layer. Upstream of the location $x/D \sim 12$, the jet leeward-side flame is generally localized, intermittent and accompanied by discontinuity due to local flame extinction. Similar to the results in $J = 0.71$, the combustion process in the downstream of interaction region between the reflected oblique shock waves and the mixing layer is promoted, followed by a typical thin reaction zone as observed by the experiments [8,21]. As seen in Figs. 10 - 12, the combustion after the shock wave is obviously enhanced, indicating that the shock waves play an important role in strengthening the combustion heat release. Moreover, intense combustion heat release appears near the wall, especially the interaction region between the shock wave and the wall.

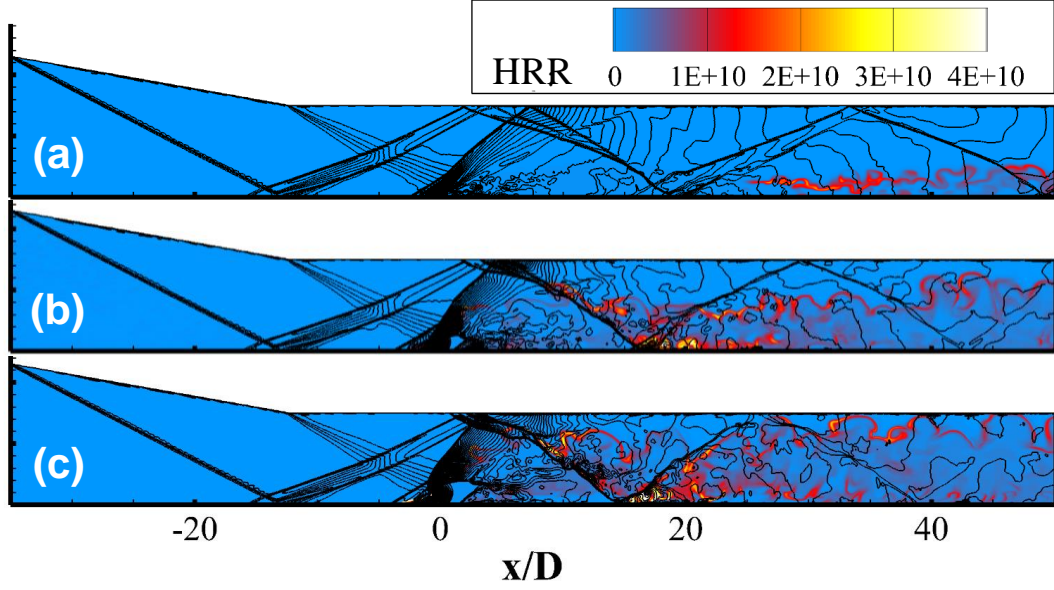


Fig. 12 Distributions of heat release rate (HRR) and pressure lined-contours (range 20KPa-800KPa) on the central lane ($z/D = 0$), where (a) $J = 0.71$, (b) $J = 2.11$ and (c) $J = 4.00$, respectively.

In order to further study the relationship between shock wave and heat release rate, an index N introduced by Moule et al. [24] is employed and defined as,

$$N = \nabla p \cdot \nabla \text{HRR} \cdot \|\text{HRR}\| / \|\text{HRR}\|_{\max}, \quad (18)$$

where, HRR is the heat release rate and $\|\text{HRR}\| / \|\text{HRR}\|_{\max}$ is used to figure out the regions of negligible heat release. The larger value of N indicates the stronger interaction between the shock and the flame. Fig. 13 provides the numerical Schlieren results and logarithmic distributions of the index N in the central plane ($z/D = 0$). The value of N behind the bow shock wave upstream of the jet exit and the reflected shock waves downstream of the jet exit is relatively high for all the three cases, which further indicates that shock waves have a strong coupling with the combustion. Meanwhile, the ignition induced by the shock occurs behind the reflected shock wave downstream of the combustion chamber for $J = 0.71$. In addition, it is worth noting that the index N in the recirculation zone upstream of the jet orifice also has relatively high values. This is mainly related to the adverse pressure gradient caused by the supersonic flow encountering the sonic fuel jet upstream of the jet orifice, which in turn forms the low-speed recirculation zone and contributes to the flame stabilization. In the supersonic transverse jet combustion system, there is a strong coupling between shock compression and heat release rates, which in turn causes ignition of the shear layer after shock/mixing layer interaction, as agreed with Moule et. al. [24] and Huete et. al. [65].

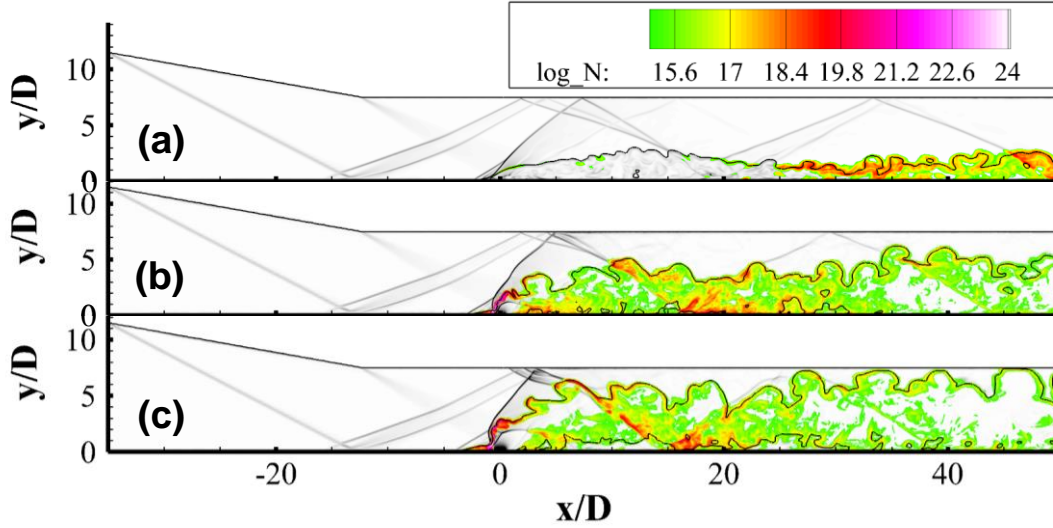


Fig. 13 Numerical schlieren results and logarithmic distributions of the index N on the central plane ($z/D = 0$), where dark line is the stoichiometric line and (a) $J = 0.71$, (b) $J = 2.11$ and (c) $J = 4.00$.

B. Ignition process

In order to study the initial ignition and flame stabilization process of supersonic transverse jet combustion after the fuel jet enters the combustion chamber, numerical simulation of the flow field without fuel jet in the combustion chamber is firstly performed to reach the statistical steady state (at t_0). Fig. 14 shows the distributions OH mass fraction and pressure contour on the central symmetry plane ($y/D = 0$) of $t - t_0 = 12\mu\text{s}$, $20\mu\text{s}$, $30\mu\text{s}$ and $40\mu\text{s}$. For the lower jet to crossflow momentum flux ratio $J = 0.71$, there is almost no reaction in the combustion chamber at $t - t_0 = 12\mu\text{s}$. It can be seen in Fig. 14(a) that the flame appears at the shear layer after the reflected shock wave at $t - t_0 = 20\mu\text{s}$. However, the compression heating of the first reflected oblique shock that the fuel jet encounters, does not provide stable combustion. As the fuel jet develops downstream ($t - t_0 = 30\mu\text{s}$ and $40\mu\text{s}$), a stable combustion flame begins to appear after the fuel jet undergoes compression heating of the second reflected oblique shock wave. For higher jet to crossflow momentum flux ratios, $J = 2.11$ and 4.00 , the fuel ignites immediately after entering the combustion chamber, and in the development of the fuel jet downstream; the first and the second reflected oblique shock waves act to strengthen the combustion, which can be seen from the apparent increase of the OH mass fraction after the shock wave. Therefore, the compression heating after the reflected oblique shock wave acts to ignite and stabilize the flame for the lower jet to crossflow momentum flux ratios, and to enhance the combustion heat release for higher jet to crossflow momentum flux ratios.

Averaged heat release rates in the initial ignition and flame stabilization process are plotted and shown in Fig. 15. The averaged heat release rate is defined as

$$Y_{HRR} = \frac{\int_V HRR dV}{\int_V dV}, \quad (19)$$

where V is the volume of the combustion chamber and HRR is the heat release rate per unit volume at the time t . According to the growth rate of the averaged heat release rate, shown in Fig. 14, the initial ignition and flame stabilization process can be roughly divided into the following three stages:

- (I) The initial stage of the fuel jet entering the combustion chamber,
- (II) Rapid growth stage of heat release rate,
- (III) Stabilization stage of heat release rate.

The corresponding time of the initial stage is approximately at $t-t_0 = 0 \sim 20\mu\text{s}$. Different ignition characteristics are observed with different jet to crossflow momentum flux ratios. For $J = 0.71$, auto-ignition is basically impossible, or auto-ignition occurs and flameout occurs immediately, and stable ignition does not occur until $t-t_0 = 20\mu\text{s}$ (as seen in Fig. 14a). For $J = 2.11$ and 4.00 , auto-ignition and stable flame occur when the fuel is injected into combustion chamber, and the averaged heat release rate increases gradually with time. The results suggest that the near-field combustion heat release rate is relatively slow with time due to the near-field mixing process but significantly affected by the jet to crossflow momentum flux ratios.

The rapid growth rate of the averaged heat release rate occurs at $t-t_0 = 20 \sim 60\mu\text{s}$, and the overall heat release rate increases with the downstream development of the fuel jet. On one hand, as in the initial stage (I), the increased contact area of the fuel jet and the supersonic crossflow increases the reaction area, thereby increasing the averaged heat release rate. On the other hand, the fuel jet and the flame of this stage will encounter reflected shock waves (including the reflected shock train formed by the combustion chamber inlet and the reflection of the bow shock), and interact with the reflected shock waves. The combustible mixture in the initial stage is heated by these shock waves, which will further promote the chemical reaction after shock waves and accelerate the growth rate of heat release at this stage. It can be clearly seen that the growth rate of the overall heat release rate in stage (II) is significantly larger than that of the initial stage (I), indicating that the reflected oblique shock wave greatly promotes the progress of the combustion chemical reaction. Although the existence of the reflected shock waves causes total pressure loss, the accelerated heat release rate can reduce the length of the supersonic combustion chamber.

In the stage (III), the overall heat release rate is stable at a certain value at $t-t_0 > 60\mu\text{s}$. The stable exothermic phase occurs at $t-t_0 > 60\mu\text{s}$ when the fuel jet flows to the exit of the combustor. At this stage, since the fuel jet

flows to the outlet, the combustion in the combustion chamber is stable, and the overall heat release rate is no longer increased. However, the steady heat release rate is still significantly affected by the jet to crossflow momentum flux ratios. Note that for the three jet to cross flux ratios, the one fuel jet flow through time defined as the time when the fuel jet enters the combustor to the outlet is about $60 \mu\text{s}$, which is smaller than the one flow through time (about $89 \mu\text{s}$).

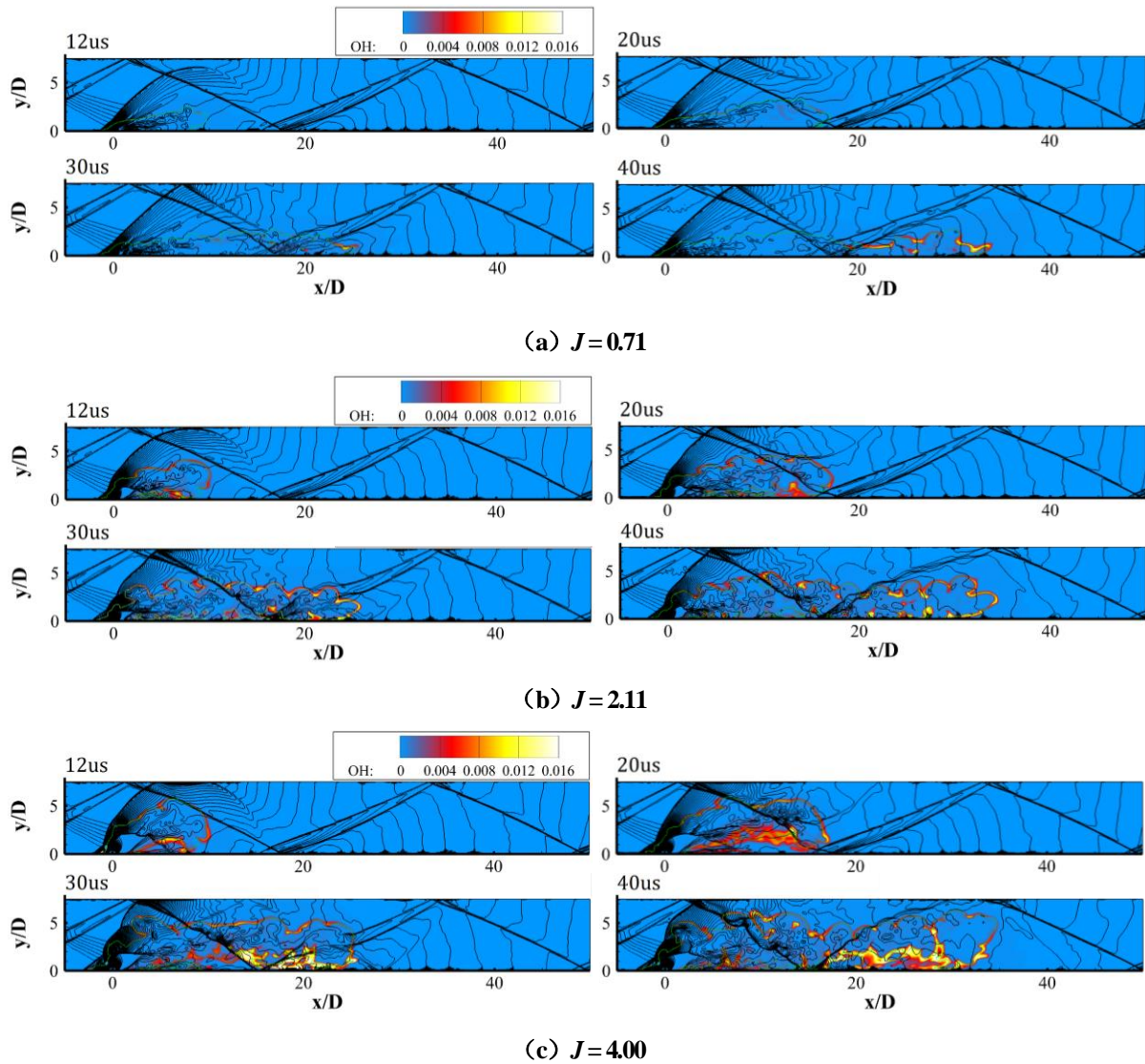


Fig. 14 Distributions of OH mass fraction and pressure lined-contours (range 20Kpa-800Kpa) on the central plane ($z/D = 0$) for (a) $J = 0.71$, (b) $J = 2.11$ and (c) $J = 4.00$, respectively.

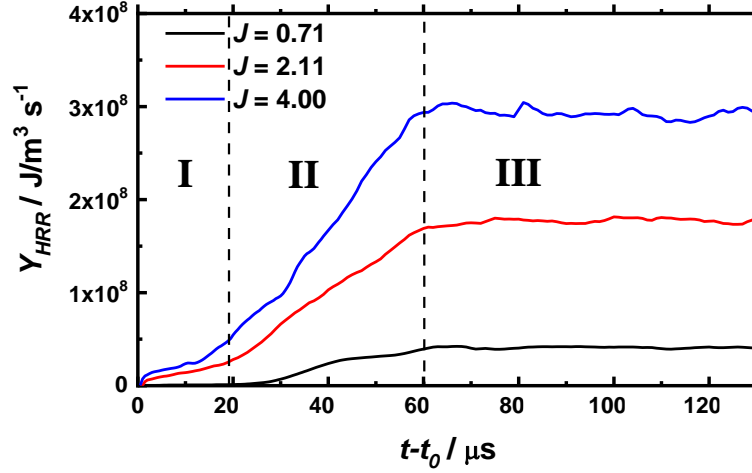


Fig. 15 Evolution of average heat release rate over time.

C. Combustion mode analysis

Takeno Flame Index (TFI) combined with heat release rates is adopted for identification of premixed or non-premixed mode in the supersonic transverse jet combustion. Takeno Flame Index is defined as [66]

$$TFI = (\nabla Y_F \cdot \nabla Y_O) / (|\nabla Y_F| |\nabla Y_O|), \quad (20)$$

where, Y_F , Y_O represent the mass fractions of hydrogen and oxidant. Fig. 16 illustrates the probability density function of TFI and the conditional average HRR on TFI at two instants, where the HRR is not less than one thousandth of the maximum HRR. Here the results of two different times are used to conform the predominant contribution mode. Results show that the combustion are mainly dominated by premixed (TFI = 1) and diffusion (TFI = -1) combustions, and that the jet to cross-flow momentum ratio has a great influence on combustion mode. For the case $J = 0.71$, the premixed combustion to overall heat release rate is the dominate mode, which is consistent with the combustion in low-speed jet in cross-flow combustor [67]. However, the formation mechanism of premixed combustion is different from that of low-velocity combustion. Under the condition of supersonic transverse jet combustion, strong interactions between the fuel jet, the wall and the cross-flow air can be observed. The mixing process is still the key limitation in the near-field combustion, so premixed combustion easily occurs in the boundary layer in the further downstream region especially for the lower J with small jet penetration height [54]. As seen in Fig. 12, although there are some combustion flames near the wall for the higher jet penetration height for $J = 2.11$ and $J = 4.00$, most of the combustion heat release rate occur on the boundary of fuel jet plume from the near field to the far field. So for the cases with higher jet to flow flux ratios $J = 2.11$ and 4.00 , the predominant contribution to the overall heat release rate comes from non-premixed combustion (TFI = -1).

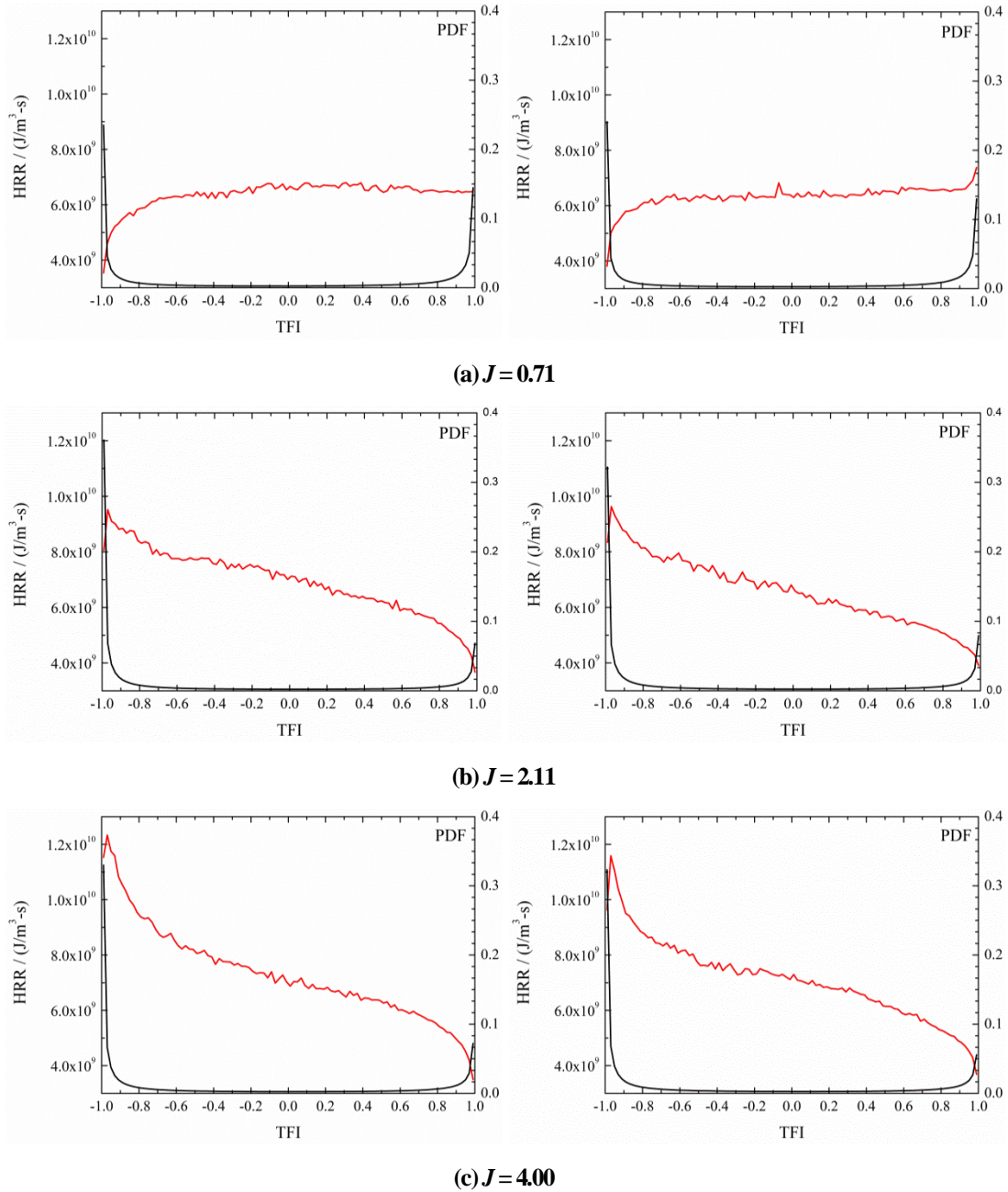


Fig. 16 The probability density function results of the conditional average TFI (black line) and the heat release rates (red line), where left is $t-t_0 = 200\mu\text{s}$, right is $t-t_0 = 400\mu\text{s}$.

D. Chemical explosive mode analysis of flame stabilization

In the supersonic transverse jet combustion with high enthalpy cross-flow, different jet to cross-flow flux ratio has an important effect on the combustion region [10]. The flame starts to anchor in the near field of the jet, mainly distributed in the shear layer after the bow shock on the windward side and the upstream recirculation zone of the jet and along the horseshoe vortex near the wall for higher jet to cross-flow flux ratio. However, the flame for the lower jet to cross-flow flux ratio case cannot anchor in the near field until the ignition by the temperature increase from the reflected shocks. In this section, the chemical explosive mode analysis (CEMA)

combined with the characteristics of a typical flame is used to analyze the auto-ignition region and the flame front, which helps to understand the mechanism of flame stabilization in the supersonic transverse jet combustion.

Based on the concept of computational singular perturbation (CSP), CEMA method proposed by Lu et al. [37] is used to identify typical combustion modes such as ignition, extinction, and premixed flame propagation front. According to the local temperature, pressure and species mass fraction, the eigenvalues of the chemical reaction source terms in the discretized conservation equations of species and temperature are analyzed. The local combustible mixture with the positive real part of eigenvalues $\text{Re}(\lambda_e) > 0$ is in chemical explosive mode (CEM), indicating the propensity of the mixture to auto-ignite, where λ_e is the first of the eigenvalues sorted in descending order with the real part. If the eigenvalue value is negative, it indicates a location with post-ignition or non-reaction mixtures. $\text{Re}(\lambda_e) = 0$ indicates the ignition point or premixed reaction front. Furthermore, the quantification contributions of species and temperature to the CEM can also be obtained in the CEMA. For turbulent combustion flows with complex mixing process, a Damköhler number defined as $\text{Da} = \text{Re}(\lambda_e) \cdot \tau_s$ is also proposed [37,68] to consider the effects of mixing process, where $\tau_s = \chi^{-1}$ is the mixing time scale and $\text{Re}(\lambda_e)$ is the reciprocal time scale of chemical explosive mode. χ is the local scalar dissipation rate based on mixture fraction as suggested in Ref. [68]. The mixture with $\text{Da} \gg 1$ is auto-igniting because the mixing process is significantly slower than the chemical explosive mode.

The flame stabilization mechanisms for typical higher jet to cross-flow flux ratios ($J = 2.11$) and lower jet to cross-flow flux ratio ($J = 0.71$) are discussed as follows. Note that the CEMA of instantaneous fields at different times has been performed and similar phenomena are observed for each jet to cross-flow flux ratios respectively. Therefore, only one instantaneous field is presented in the following discussions. In addition, the CEMA of jet to cross-flow flux ratio $J = 4.00$ has the similar results with that of $J = 2.11$ and will be not shown here.

1) Jet to cross-flow flux ratio $J = 2.11$

Figure 17 shows the distributions of temperature, mass fraction of OH, H, HO₂, TFI, contribution of radical H to the CEM, the logarithmic distribution of $\text{Re}(\lambda_e)$ and the Da number defined by CEMA in the central plane ($z/D = 0$). The presence of flame can be characterized by the intermediate radical OH and H. In addition, it can be seen from Fig. 17 that high HO₂ mass fraction is mainly distributed in the fuel-rich side of the hydrogen jet plume, which is consistent with DNS results of low-speed hydrogen jet combustion by Lu et al. [37]. Boivin et al. [69] pointed out that combining the production rate of HO₂ with the reactivity of the mixture in the flow field can determine whether the local combustion is auto-ignition process. Therefore, the intermediate radical HO₂ can be

used as a criterion of auto-ignition in the hydrogen/air combustion field. The CEM mainly occurs in the near-field region of supersonic transverse hydrogen jet combustion within $Re(\lambda_e) \gg 0$ and $Da \gg 1$. It can be found that the region with high HO_2 produced is mainly consistent with the distribution region of CEM.

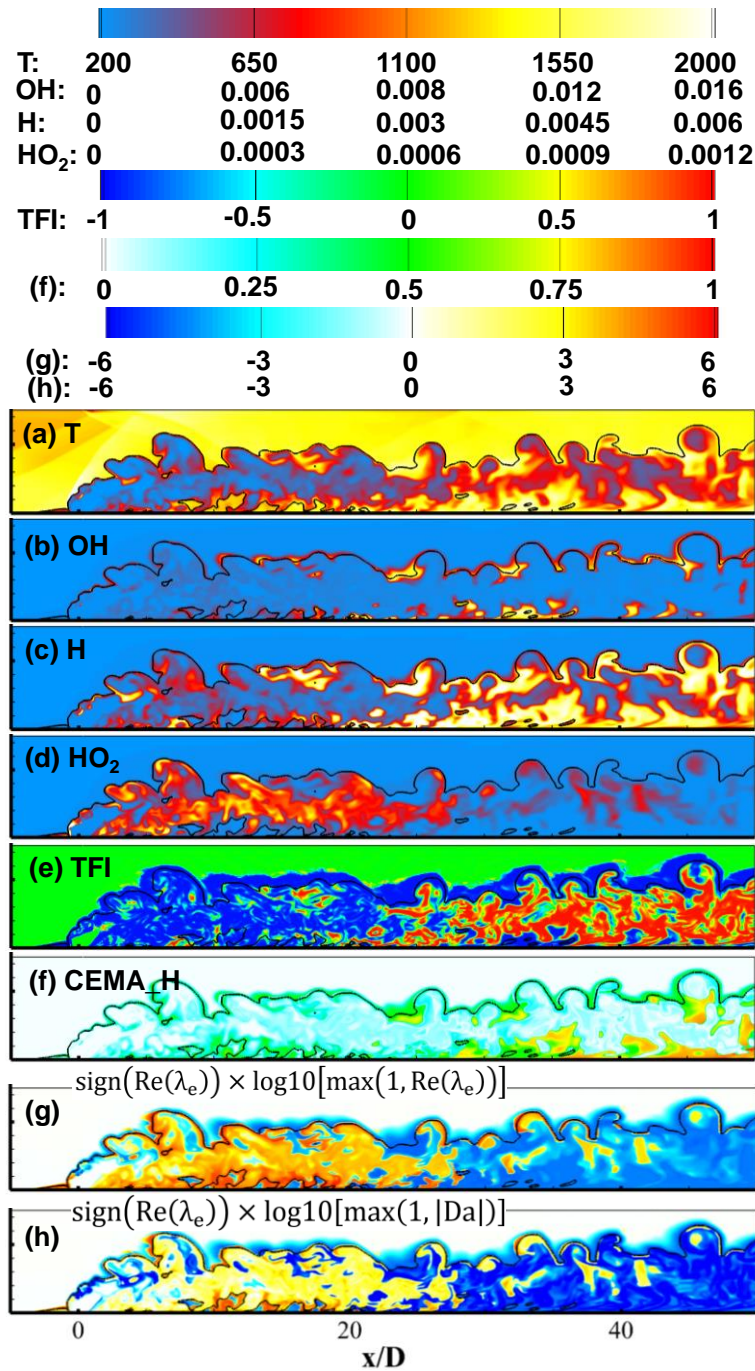


Fig. 17 Distributions of combustion field and CEMA results on the central plane ($z/D = 0$), with dark stoichiometric line, for case $J = 2.11$.

Furthermore, distributions of instantaneous combustion flow field in the near field of hydrogen injection are shown in Fig. 18, including the heat release rate, intermediate reaction radical H, intermediate reaction radical OH, density and temperature. Intense combustion heat release rate occurs in the shear layer behind the windward

bow shock, where the local temperature is very high due to the compression heating of the shock wave (see the distributions of density and temperature in Fig. 18). As the jet shear layer developed downstream, local extinction and re-ignition appear in the windward shear layer, which is consistent with the observations in the experiment by Gamba et al. [7]. In addition, combustion also appears in the recirculation zone upstream of the jet orifice, which is related to the flame stabilization in the supersonic transverse jet combustion at higher jet to cross-flow flux ratios.

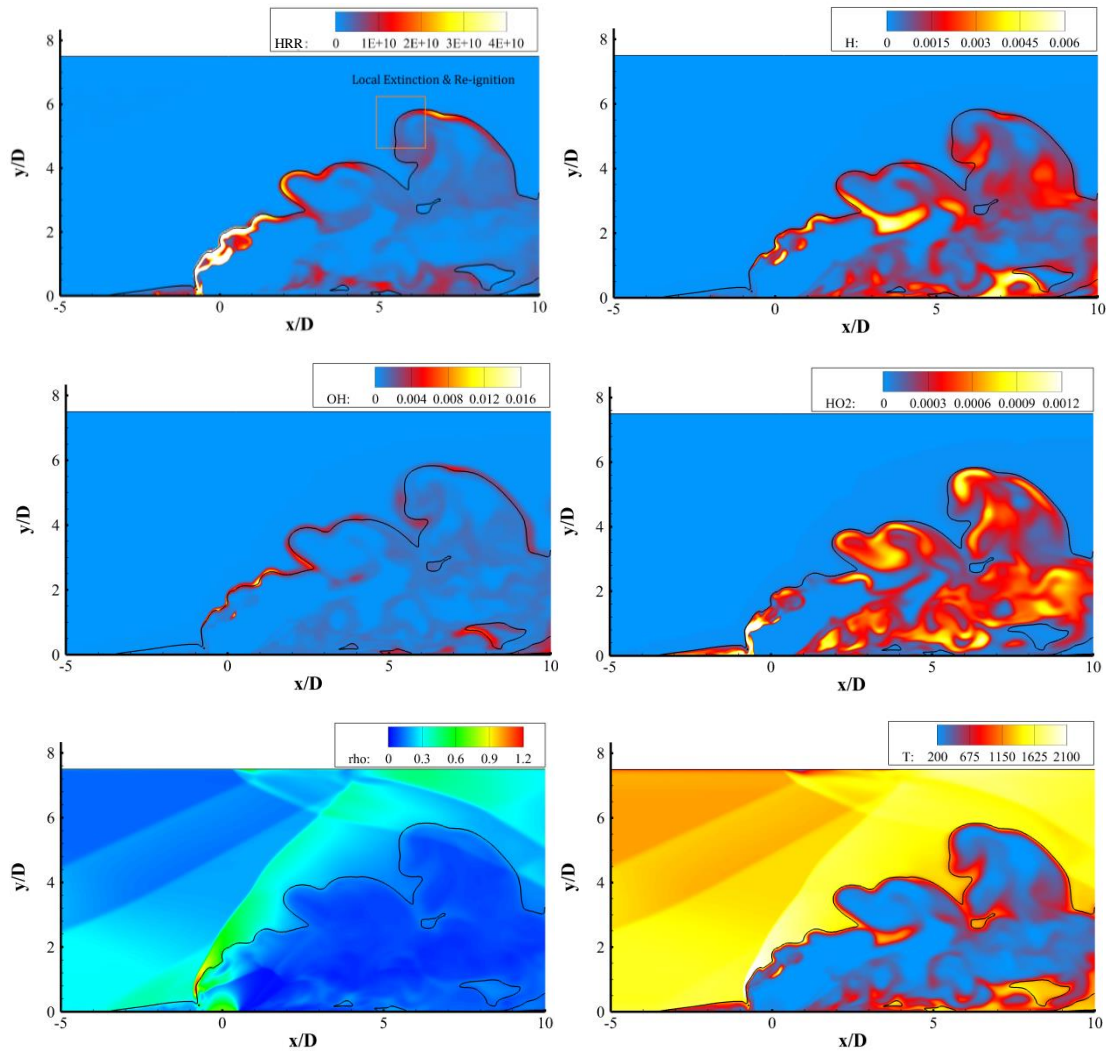


Fig. 18 Distributions of instantaneous combustion field in the near field of fuel jet on the central plane ($z/D = 0$), with dark stoichiometric line, for case $J = 2.11$.

Figure 19 shows the CEMA result and the distribution of TFI for the corresponding positions in Fig. 18. The CEM $Re(\lambda_e) > 0$ is mainly in the recirculation zone, the windward side and leeward side shear layer close to the fuel jet. Combined the distribution of Da number in the CEM region, especially for the region in the recirculation zone and the foot of the bow shock, where Da number is much greater than 1. Therefore, it can be concluded that the flame stabilization mechanism in such regions is auto-ignition. Whereas that the region where the Da number

is much smaller than unit is a typical diffusion flame region [68]. The Da number in the windward shear layer regions, where the local extinction and re-ignition, as seen Fig. 18, is greater than 1, indicating that the mixing time scale here is much larger than the chemical reaction time scale. The chemical reaction in the re-ignition region is CEM and dominated by the mixing process, so the re-ignition is a process of auto-ignition. The contribution of radical H to the CEM in the chemical reaction is also shown in Fig. 19. The radical H contributes more than 0.5 to the combustible mixture of CEM in the foot of the bow shock. Large amounts of production of the intermediate radical H plays a crucial role on auto-ignition, further indicating that flame in the foot of bow shock is auto-ignition. Moreover, the distribution of TFI suggests that the combustion flame is mixing dominant in the near field of hydrogen injection.

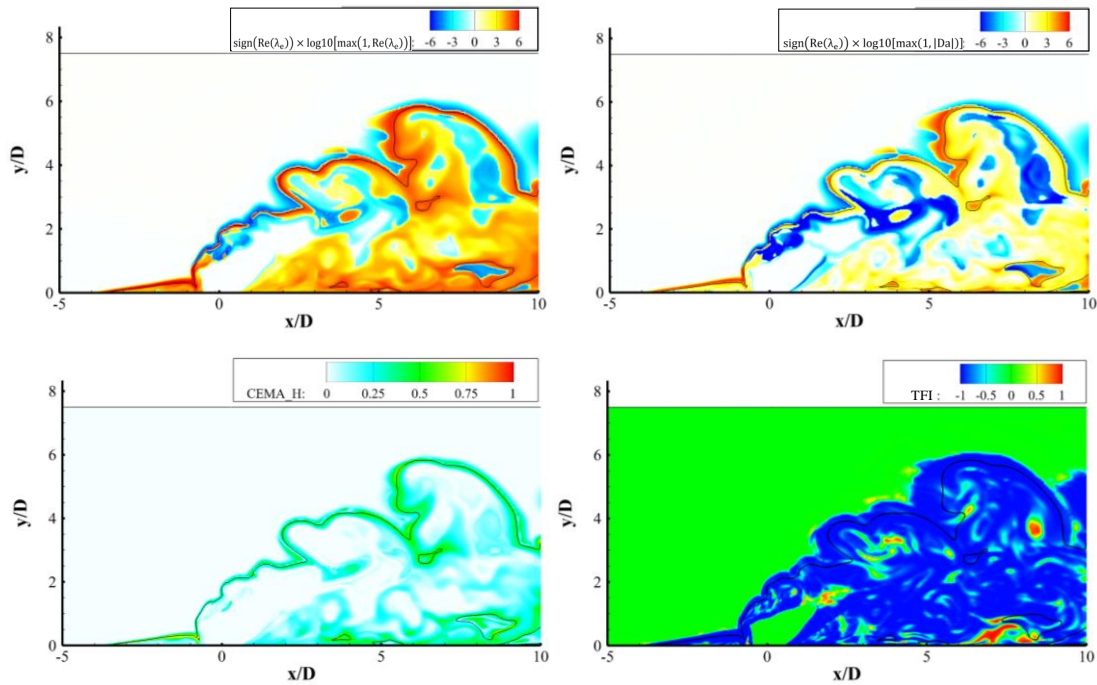


Fig. 19 The combustion field and CEMA results in the near field of fuel jet on the central plane ($z/D = 0$), with dark stoichiometric line, for case $J = 2.11$.

Figure 20 shows the instantaneous combustion field including heat release rate, radical H mass fraction, radical OH mass fraction, and temperature on the plane of $y/D = 0.25$ near the bottom wall. The combustion flame near the wall of supersonic transverse jet combustion exhibits distributed like reaction zone regime, which is also clearly captured in the experiment of Gamba et al. [8,10]. The CMEA results and the distribution of TFI corresponding in Fig. 20 are shown in Fig. 21. It is observed that the CEM near the wall region is significantly changed due to the interaction between the reflected shock wave, fuel jet plume and boundary layers. Combustible mixtures along the horseshoe vortex region upstream of the shock/boundary layer recirculation zone are in CEM, while intense combustion with non-CEM are observed in the recirculation zone, as seen in [55] and in the far-

field downstream ($x/D > 16$). The Da number is smaller than 1, indicating that the combustion in such region is mixing-dominated diffusion flame. It is further shown that the reflected shock wave interacting with the jet plume and the boundary layer can enhance the combustion with higher jet to cross-flow flux ratio. Combined with the distribution of the Da number, $Re(\lambda_e)$ of CEMA results and TFI, it can be concluded that the flame near the field along the horseshoe region is a mixing dominated distributed reaction zone induced by auto-ignition.

It should be noted that although the CEMA of jet to cross-flow flux ratio $J = 4.00$ has similar results with that of $J = 2.11$ as discussed above, there are still some differences between the results of CEMA. For instance, the upstream recirculation zone in the state of CEM (i.e. $Re(\lambda_e) > 0$) of $J = 4.00$ is larger than that of $J = 2.11$, and the mixing dominated distributed reaction zone induced by auto-ignition for $J = 4.00$ is much broader than that for $J = 2.11$ in the near field along the horseshoe region.

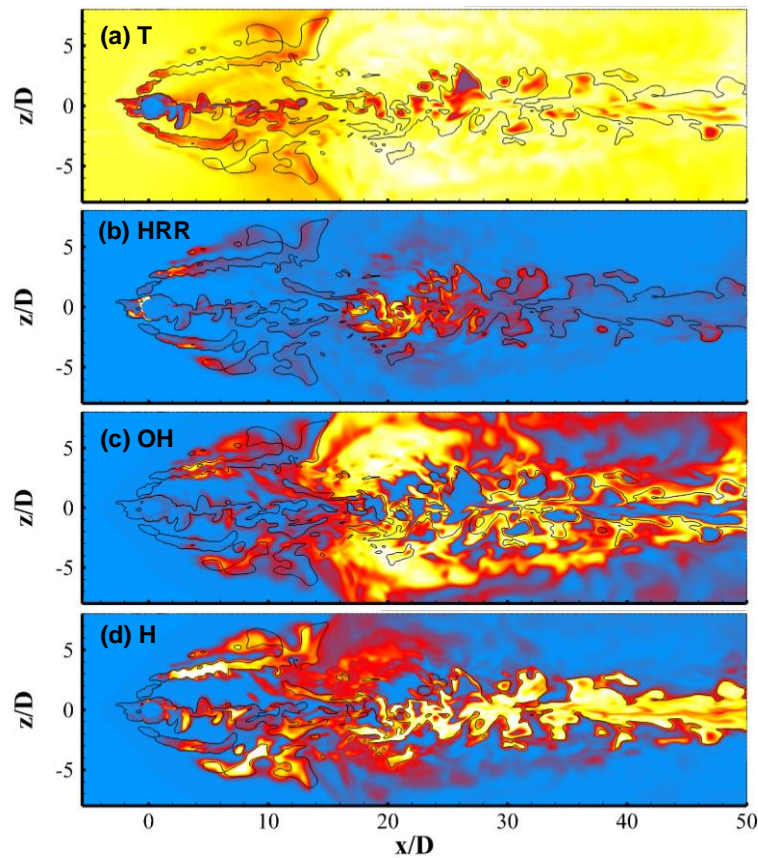


Fig. 20 The instantaneous combustion field in the plane of $y/D = 0.25$ near the wall, with dark stoichiometric line and color bar shown in Fig. 18, for case $J = 2.11$.

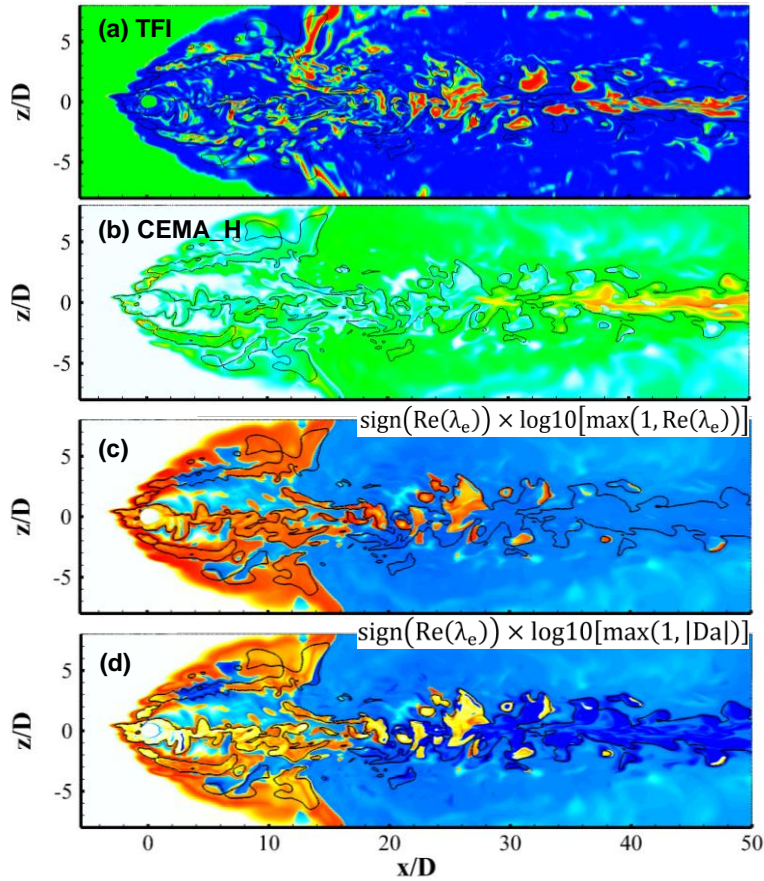


Fig. 21 Distributions of the combustion field and CEMA results on the plane of $y/D = 0.25$, with dark stoichiometric line and color bar shown in Fig. 17, for case $J = 2.11$.

2) Jet to cross-flow flux ratio $J = 0.71$

Figure 22 shows distributions of the combustion field information, CEMA results and the TFI in the central plane ($z/D = 0$) for $J = 0.71$. The combustion flame appears in the shear layer downstream far field of the jet orifice, which can be seen with the heat release rate, H mass fraction and OH mass fraction in the central plane ($y/D = 0$). According to CEMA, the combustible mixture is in CEM and the Da number is much larger than 1 in the shear layer, which suggest that the flame in the downstream shear layer is due to auto-ignition.

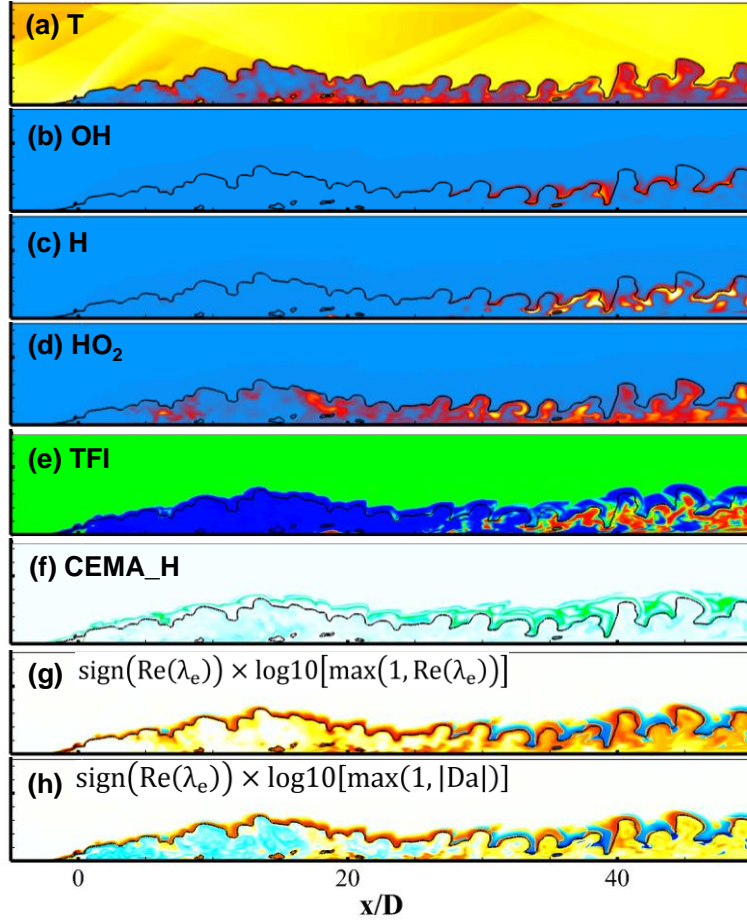


Fig. 22 Distributions of the combustion field and CEMA results on the central plane ($z/D = 0$), with dark stoichiometric line and color bar shown in Fig. 17, for case $J = 0.71$.

Similarly, the combustion near the wall is analysed for $J = 0.71$. Figs. 23 and 24 show the near wall distributions of combustion field, CEMA results and TFI, respectively ($y/D = 0.25$). No flame is observed on either side of the horseshoe in the near wall region, near the fuel jet orifice. The combustion flame occurs and anchors in the symmetrical recirculation zone region of $10 < x/D < 20$ due to the interaction of reflected shock wave, the jet plume and the boundary layer. The flame is also mixing dominated in the view of TFI. It is noteworthy that intense heat release rate (HRR) occurs near the wall in the premix region, identified by the TFI being greater than zero. The flame shows similar to the jet lifting flame [10]. By comparing the distributions of the Da number and $\text{Re}(\lambda_e)$ of CEMA results in the near wall, the flame stabilization mechanism in the supersonic transverse jet combustion with low jet to cross-flow flux ratio can be clearly identified as auto-ignition.

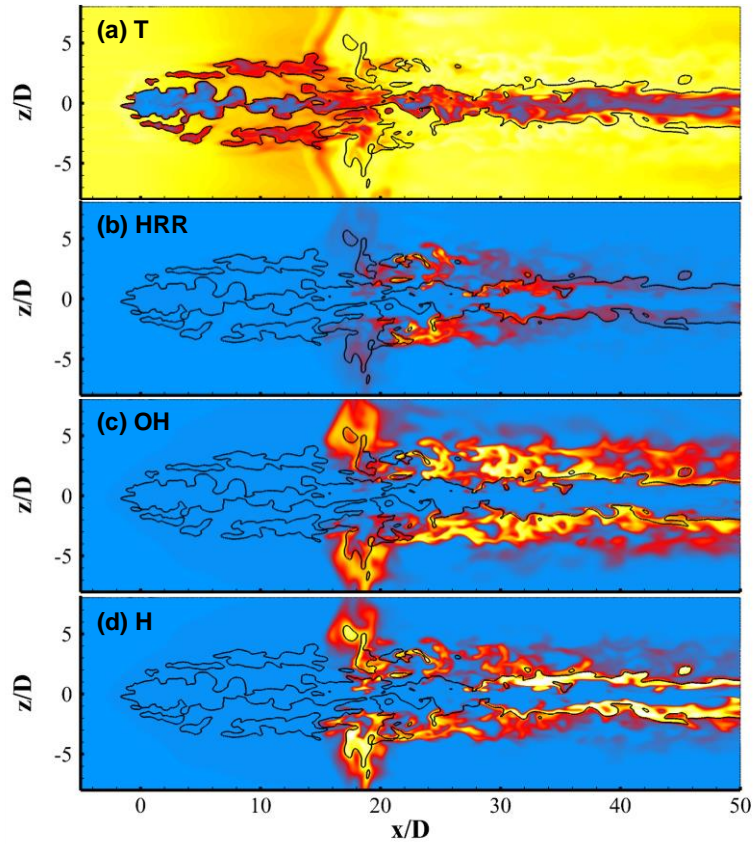


Fig. 23 The instantaneous combustion field on the plane of $y/D = 0.25$ near the wall, with dark stoichiometric line and color bar shown in Fig. 18, for case $J = 0.71$.

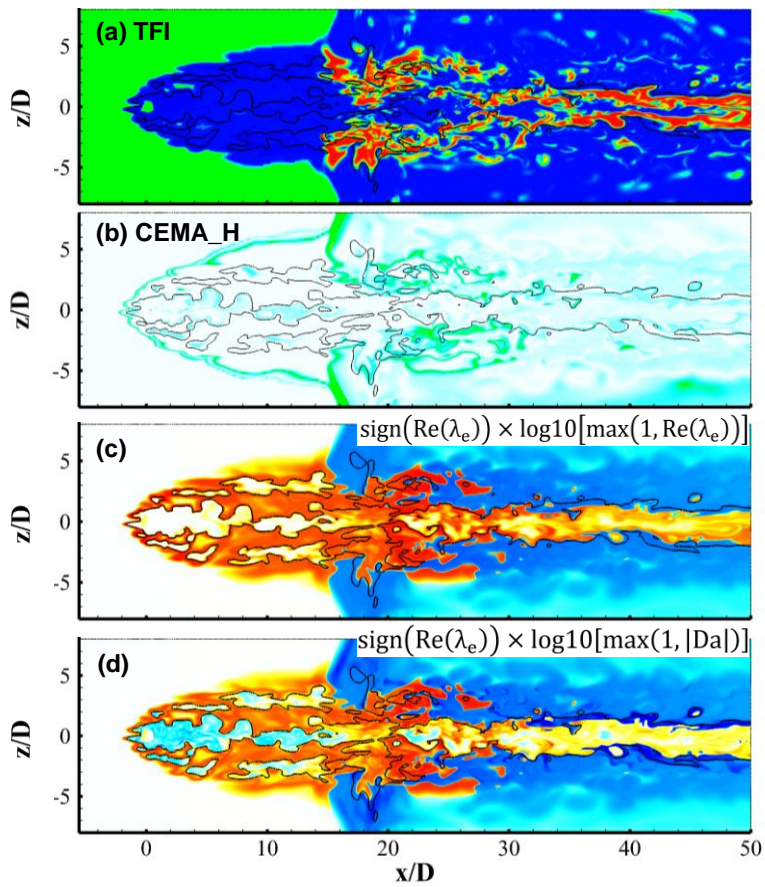


Fig. 24 The combustion field information and CEMA results on the plane of $y/D = 0.25$, with dark stoichiometric line and color bar shown in Fig. 17, for case $J = 0.71$.

IV. Conclusion

Large-eddy simulations combined with PaSR sub-grid combustion model have been performed to investigate mixing, combustion mode and flame stability in a high-enthalpy JISCF combustor. The present work is focused on the effects of J on the flame stability and combustion process of JISCF with an inlet ramp. Three levels of grid refinement are used to access the mesh sensitivity analysis. The numerical methods and mesh resolution are validated by comparison with the experimental data and by further analyzing various resolution criteria with the fine mesh.

Due to existence of shock trains generated in the scramjet engine combustion chamber, the heat release rate after the shock wave is significantly increased, which indicates a strong coupling of shock waves and chemical reactions. The shock induced ignition is observed after the reflected shock wave for case $J = 0.71$. However, the shock induced ignitions happen toward around the jet orifice for cases $J = 2.11$ and 4.00 , for which the bow shock wave and the recirculation zone upstream of the jet orifice contribute to auto-ignition and flame anchoring. The combustion mode analysis indicates that the combustion heat release is dominated by premixed combustion for the low jet to cross-flow momentum flux ratio, $J = 0.71$. While for the high jet to cross-flow momentum flux ratios, $J = 2.11$ and 4.00 , the combustion heat release is dominated by non-premixed combustion.

From the chemical explosive mode analysis, two main types of flame stabilization mechanism are identified, i.e. the shock induced high temperature auto-ignition for the low J (0.71) and the mixing dominated auto-ignition along the horseshoe vortex region and the upwind jet shear layer for high J (i.e. 2.11 and 4.00). In addition, flame along the horseshoe vortex region exhibits mixing dominated distributed reaction zones in the near field of jet orifice of $J = 2.11$ and 4.00 , which are induced by auto-ignitions. The combustion in the recirculation zone formed by interactions between the reflected shock wave and boundary layer is mixing-dominated diffusion combustion.

Acknowledgment

This work is supported by the National Natural Science Foundation of China (Grant No. 51576182 and Grant No. 91441117). The numerical simulations in this paper have been performed on the supercomputers in the Supercomputing Center, University of Science and Technology of China. We thank Professor Ren Zhuyin and Dr. Wu Wantong at Tsinghua University for helpful discussions on CEMA.

References

- [1] Karagozian, A. R. “Transverse Jets and Their Control.” *Progress in energy and combustion science*, Vol. 36, No. 5, 2010, pp. 531–553.

<https://doi.org/10.1016/j.pecs.2010.01.001>

- [2] Mahesh, K. “The Interaction of Jets with Crossflow.” *Annual Review of Fluid Mechanics*, Vol. 45, No. 1, 2013, pp. 379–407.

<https://doi.org/10.1146/annurev-fluid-120710-101115>

- [3] Huang, W. “Transverse Jet in Supersonic Crossflows.” *Aerospace Science and Technology*, Vol. 50, 2016, pp. 183–195.

<https://doi.org/10.1016/j.ast.2016.01.001>

- [4] Scherrer, D., Dessornes, O., Ferrier, M., Vincent-Randonnier, A., Moule, Y., and Sabel’Nikov, V. “Research on Supersonic Combustion and Scramjet Combustors at ONERA.” *AerospaceLab*, No. 11, 2015, p. 4.

- [5] Rana, Z. A., Thornber, B., and Drikakis, D. “Transverse Jet Injection into a Supersonic Turbulent Cross-Flow.” *Physics of Fluids*, Vol. 23, No. 4, 2011, p. 46103.

<https://doi.org/10.1063/1.3570692>

- [6] Smart, M. K., Hass, N. E., and Paull, A. “Flight Data Analysis of the HyShot 2 Scramjet Flight Experiment.” *AIAA journal*, Vol. 44, No. 10, 2006, pp. 2366–2375.

<https://doi.org/10.2514/1.20661>

- [7] Hass, N., Smart, M., and Paull, A. Flight Data Analysis of the HYSHOT 2. 2005.

<https://doi.org/10.2514/6.2005-3354>

- [8] Gamba, M., Miller, V., Mungal, M. G., and Hanson, R. Ignition and Flame Structure in a Compact Inlet/Scramjet Combustor Model. 2011.

<https://doi.org/10.2514/6.2011-2366>

[9] Gamba, M., Mungal, M. G., and Hanson, R. Ignition and Near-Wall Burning in Transverse Hydrogen Jets in Supersonic Crossflow. 2011.

<https://doi.org/10.2514/6.2011-319>

[10] Gamba, M., and Mungal, M. G. “Ignition, Flame Structure and near-Wall Burning in Transverse Hydrogen Jets in Supersonic Crossflow.” *Journal of Fluid Mechanics*, Vol. 780, 2015, pp. 226–273.

<https://doi.org/10.1017/jfm.2015.454>

[11] Mai, T., Sakimitsu, Y., Nakamura, H., Ogami, Y., Kudo, T., and Kobayashi, H. “Effect of the Incident Shock Wave Interacting with Transversal Jet Flow on the Mixing and Combustion.” *Proceedings of the Combustion Institute*, Vol. 33, No. 2, 2011, pp. 2335–2342.

<https://doi.org/10.1016/j.proci.2010.07.056>

[12] Laurence, S. J., Lieber, D., Schramm, J. M., Hannemann, K., and Larsson, J. “Incipient Thermal Choking and Stable Shock-Train Formation in the Heat-Release Region of a Scramjet Combustor. Part I: Shock-Tunnel Experiments.” *Combustion and Flame*, Vol. 162, No. 4, 2015, pp. 921–931.

<https://doi.org/10.1016/j.combustflame.2014.09.016>

[13] Sun, M., and Hu, Z. “Mixing in Nearwall Regions Downstream of a Sonic Jet in a Supersonic Crossflow at Mach 2.7.” *Physics of Fluids*, Vol. 30, No. 10, 2018, p. 106102.

<https://doi.org/10.1063/1.5045752>

[14] Liu, C., Yu, J., Wang, Z., Sun, M., Wang, H., and Grosshans, H. “Characteristics of Hydrogen Jet Combustion in a High-Enthalpy Supersonic Crossflow.” *Physics of Fluids*, Vol. 31, No. 4, 2019, p. 46105.

<https://doi.org/10.1063/1.5084751>

[15] Du, Z., Huang, W., Yan, L., and Li, S. “Reynolds-Average Navier-Stokes Study of Steady and Pulsed Gaseous Jets with Different Periods for the Shock-Induced Combustion Ramjet Engine.” *Physics of Fluids*, Vol. 31, No. 5, 2019, p. 55107.

<https://doi.org/10.1063/1.5097238>

[16] Urzay, J. “Supersonic Combustion in Air-Breathing Propulsion Systems for Hypersonic Flight.” *Annual Review of Fluid Mechanics*, Vol. 50, 2018, pp. 593–627.

<https://doi.org/10.1146/annurev-fluid-122316-045217>

[17] Gonzalez-Juez, E. D., Kerstein, A. R., Ranjan, R., and Menon, S. “Advances and Challenges in Modeling High-Speed Turbulent Combustion in Propulsion Systems.” *Progress in Energy and Combustion Science*, Vol. 60, 2017, pp. 26–67.

<https://doi.org/10.1016/j.pecs.2016.12.003>

[18] Ben-Yakar, A. Experimental Investigation of Mixing and Ignition of Transverse Jets in Supersonic Crossflows. 2000.

[19] Fureby, C., Chapuis, M., Fedina, E., and Karl, S. “CFD Analysis of the HyShot II Scramjet Combustor.” *Proceedings of the Combustion Institute*, Vol. 33, No. 2, 2011, pp. 2399–2405.

<https://doi.org/10.1016/j.proci.2010.07.055>

[20] Chapuis, M., Fedina, E., Fureby, C., Hannemann, K., Karl, S., and Schramm, J. M. “A Computational Study of the HyShot II Combustor Performance.” *Proceedings of the Combustion Institute*, Vol. 34, No. 2, 2013, pp. 2101–2109.

<https://doi.org/10.1016/j.proci.2012.07.014>

[21] Gamba, M., Miller, V., Mungal, G., and Hanson, R. Combustion Characteristics of an Inlet/Supersonic Combustor Model. 2012.

<https://doi.org/10.2514/6.2012-612>

[22] Luo, K., Jin, T., Lu, S., and Fan, J. “DNS Analysis of a Three-Dimensional Supersonic Turbulent Lifted Jet Flame.” *Fuel*, Vol. 108, 2013, pp. 691–698.

<https://doi.org/10.1016/j.fuel.2013.02.050>

[23] Fureby, C., Nordin-Bates, K., Petterson, K., Bresson, A., and Sabelnikov, V. “A Computational Study of Supersonic Combustion in Strut Injector and Hypermixer Flow Fields.” *Proceedings of the Combustion Institute*, Vol. 35, No. 2, 2015, pp. 2127–2135.

<https://doi.org/10.1016/j.proci.2014.06.113>

- [24] Moule, Y., Sabelnikov, V., and Mura, A. “Highly Resolved Numerical Simulation of Combustion in Supersonic Hydrogen–Air Coflowing Jets.” *Combustion and Flame*, Vol. 161, No. 10, 2014, pp. 2647–2668.

<https://doi.org/10.1016/j.combustflame.2014.04.011>

- [25] Ghodke, C., Choi, J., Srinivasan, S., and Menon, S. Large Eddy Simulation of Supersonic Combustion in a Cavity-Strut Flameholder. 2011.

<https://doi.org/10.2514/6.2011-323>

- [26] Edwards, J., Potturi, A., and Fulton, J. Large Eddy/Reynolds-Averaged Navier-Stokes Simulations of Scramjet Combustor Flow Fields. 2012.

<https://doi.org/10.2514/6.2012-4262>

- [27] Saghafian, A., Terrapon, V. E., and Pitsch, H. “An Efficient Flamelet-Based Combustion Model for Compressible Flows.” *Combustion and Flame*, Vol. 162, No. 3, 2015, pp. 652–667.

<https://doi.org/10.1016/j.combustflame.2014.08.007>

- [28] Saghafian, A., Shunn, L., Philips, D. A., and Ham, F. “Large Eddy Simulations of the HIFiRE Scramjet Using a Compressible Flamelet/Progress Variable Approach.” *Proceedings of the Combustion Institute*, Vol. 35, No. 2, 2015, pp. 2163–2172.

<https://doi.org/10.1016/j.proci.2014.10.004>

- [29] Poludnenko, A. Y., and Oran, E. S. “The Interaction of High-Speed Turbulence with Flames: Global Properties and Internal Flame Structure.” *Combustion and Flame*, Vol. 157, No. 5, 2010, pp. 995–1011.

<https://doi.org/10.1016/j.combustflame.2009.11.018>

- [30] Ochs, B. A., Fries, D., Scarborough, D. E., and Menon, S. Growth Rate and Flame Structure of Turbulent Premixed Flame Kernels in Supersonic Flows. 2016.

<https://doi.org/10.2514/6.2016-0440>

[31] O'Brien, J., Urzay, J., Ihme, M., Moin, P., and Saghafian, A. "Subgrid-Scale Backscatter in Reacting and Inert Supersonic Hydrogen–Air Turbulent Mixing Layers." *Journal of Fluid Mechanics*, Vol. 743, 2014, pp. 554–584.

<https://doi.org/10.1017/jfm.2014.62>

[32] Zhao, M., Li, Q., and Ye, T. "Investigation of the Mixing Characteristics in a Transverse Hydrogen Injection Combustor with an Inlet Compression Ramp." *Acta Astronautica*, Vol. 160, 2019, pp. 479–488.

<https://doi.org/10.1016/j.actaastro.2019.02.026>

[33] Wang, H., Shan, F., Piao, Y., Hou, L., and Niu, J. "IDDES Simulation of Hydrogen-Fueled Supersonic Combustion Using Flamelet Modeling." *International Journal of Hydrogen Energy*, 2015.

<https://doi.org/10.1016/j.ijhydene.2014.10.124>

[34] Candler, G. V., Cymbalist, N., and Dimotakis, P. E. "Wall-Modeled Large-Eddy Simulation of Autoignition-Dominated Supersonic Combustion." *Aiaa Journal*, Vol. 55, No. 7, 2017, pp. 2410–2423.

<https://doi.org/10.2514/1.J055550>

[35] Bouheraoua, L., Domingo, P., and Ribert, G. "Large-Eddy Simulation of a Supersonic Lifted Jet Flame: Analysis of the Turbulent Flame Base." *Combustion and Flame*, Vol. 179, 2017, pp. 199–218.

<https://doi.org/10.1016/j.combustflame.2017.01.020>

[36] Berglund, M., Fedina, E., Fureby, C., Tegnér, J., and Sabel'nikov, V. "Finite Rate Chemistry Large-Eddy Simulation of Self-Ignition in Supersonic Combustion Ramjet." *AIAA Journal*, Vol. 48, No. 3, 2010, pp. 540–550.

<https://doi.org/10.2514/1.43746>

[37] Lu, T. F., Yoo, C. S., Chen, J. H., and Law, C. K. "Three-Dimensional Direct Numerical Simulation of a Turbulent Lifted Hydrogen Jet Flame in Heated Coflow: A Chemical Explosive Mode Analysis." *Journal of Fluid Mechanics*, Vol. 652, 2010, pp. 45–64.

<https://doi.org/10.1017/S002211201000039X>

[38] Poling, B. E., Prausnitz, J. M., and O'Connell, J. P. *The Properties of Gases and Liquids*. McGraw-hill New York, 2001.

[39] McBride, B. J. *Coefficients for Calculating Thermodynamic and Transport Properties of Individual Species*. National Aeronautics and Space Administration, Office of Management, 1993.

[40] Nicoud, F., and Ducros, F. "Subgrid-Scale Stress Modelling Based on the Square of the Velocity Gradient Tensor." *Flow, turbulence and Combustion*, Vol. 62, 1999, pp. 183–200.

<https://doi.org/10.1023/A:1009995426001>

[41] Piscaglia, F., Montorfano, A., and Onorati, A. "Towards the LES Simulation of IC Engines with Parallel Topologically Changing Meshes." *SAE International Journal of Engines*, Vol. 6, No. 2, 2013, pp. 926–940.

<https://www.jstor.org/stable/26277672>

[42] Cao, C., Ye, T., and Zhao, M. "Large Eddy Simulation of Hydrogen/Air Scramjet Combustion Using Tabulated Thermo-Chemistry Approach." *Chinese Journal of Aeronautics*, Vol. 28, No. 5, 2015.

<https://doi.org/10.1016/j.cja.2015.08.008>

[43] Sabelnikov, V., and Fureby, C. "LES Combustion Modeling for High Re Flames Using a Multi-Phase Analogy." *Combustion and Flame*, Vol. 160, No. 1, 2013, pp. 83–96.

<https://doi.org/10.1016/j.combustflame.2012.09.008>

[44] Fureby, C. A Comparative Study of Subgrid Models, Reaction Mechanisms and Combustion Models in LES of Supersonic Combustion. 2019.

<https://doi.org/10.2514/6.2019-4273>

[45] Berglund, M., and Fureby, C. "LES of Supersonic Combustion in a Scramjet Engine Model." *Proceedings of the Combustion Institute*, Vol. 31, No. 2, 2007, pp. 2497–2504.

<https://doi.org/10.1016/j.proci.2006.07.074>

[46] Berglund, M., Fedina, E., Fureby, C., Tegnér, J., and Sabel'nikov, V. "Finite Rate Chemistry Large-Eddy Simulation of Self-Ignition in Supersonic Combustion Ramjet." *AIAA Journal*, Vol. 48, No. 3, 2010, pp. 540–550.

<https://doi.org/10.2514/1.43746>

[47] Jachimowski, C. J. "An Analytical Study of the Hydrogen-Air Reaction Mechanism with Application to Scramjet Combustion." 1988.

[48] Slack, M., and Grillo, A. "Investigation of Hydrogen-Air Ignition Sensitized by Nitric Oxide and by Nitrogen Dioxide." 1977.

[49] Kwon, O. C., and Faeth, G. M. "Flame/Stretch Interactions of Premixed Hydrogen-Fueled Flames: Measurements and Predictions." *Combustion and Flame*, Vol. 124, No. 4, 2001, pp. 590–610.

[https://doi.org/10.1016/S0010-2180\(00\)00229-7](https://doi.org/10.1016/S0010-2180(00)00229-7)

[50] Juniper, M., Darabiha, N., and Candel, S. "The Extinction Limits of a Hydrogen Counterflow Diffusion Flame above Liquid Oxygen." *Combustion and flame*, Vol. 135, No. 1–2, 2003, pp. 87–96.

[https://doi.org/10.1016/S0010-2180\(03\)00149-4](https://doi.org/10.1016/S0010-2180(03)00149-4)

[51] Zhao, M., Li, J.-M., Teo, C. J., Khoo, B. C., and Zhang, H. "Effects of Variable Total Pressures on Instability and Extinction of Rotating Detonation Combustion." *Flow, Turbulence and Combustion*, 2019, pp. 1–30.

<https://doi.org/10.1007/s10494-019-00050-y>

[52] Jasak, H., Jemcov, A., and Tukovic, Z. OpenFOAM: A C++ Library for Complex Physics Simulations. No. 1000, 2007, pp. 1–20.

[53] Hoffmann, K. A., and Chiang, S. T. "Computational Fluid Dynamics Volume I." *Engineering Education System*, 2000.

[54] Zhao, M., Ye, T., Cao, C., Zhou, T., and Zhu, M. "Study of Sonic Injection from Circular Injector into a Supersonic Cross-Flow Using Large Eddy Simulation." *International Journal of Hydrogen Energy*, Vol. 41, No. 39, 2016.

<https://doi.org/10.1016/j.ijhydene.2016.07.018>

[55] Zhao, M., Zhou, T., Ye, T., Zhu, M., and Zhang, H. “Large Eddy Simulation of Reacting Flow in a Hydrogen Jet into Supersonic Cross-Flow Combustor with an Inlet Compression Ramp.” *International Journal of Hydrogen Energy*, Vol. 42, No. 26, 2017.

<https://doi.org/10.1016/j.ijhydene.2017.04.250>

[56] Peterson, D. M., and Candler, G. V. “Hybrid Reynolds-Averaged and Large-Eddy Simulation of Normal Injection into a Supersonic Crossflow.” *Journal of Propulsion and Power*, Vol. 26, No. 3, 2010, pp. 533–544.

<https://doi.org/10.2514/1.46810>

[57] Wang, G., Chen, L., and Lu, X. “Effects of the Injector Geometry on a Sonic Jet into a Supersonic Crossflow.” *Science China Physics, Mechanics and Astronomy*, Vol. 56, No. 2, 2013, pp. 366–377.

<https://doi.org/10.1007/s11433-012-4984-2>

[58] Bodony, D. J., and Lele, S. K. “On Using Large-Eddy Simulation for the Prediction of Noise from Cold and Heated Turbulent Jets.” *Physics of Fluids*, Vol. 17, No. 8, 2005, p. 85103.

<https://doi.org/10.1063/1.2001689>

[59] Pope, S. B. *Turbulent Flows*. 2001.

[60] Kawai, S., and Lele, S. K. “Large-Eddy Simulation of Jet Mixing in Supersonic Crossflows.” *AIAA journal*, Vol. 48, No. 9, 2010, pp. 2063–2083.

<https://doi.org/10.2514/1.J050282>

[61] Xia, Z., Han, X., and Mao, J. “Assessment and Validation of Very-Large-Eddy Simulation Turbulence Modeling for Strongly Swirling Turbulent Flow.” *AIAA Journal*, Vol. 58, No. 1, 2020, pp. 148–163.

<https://doi.org/10.2514/1.J058302>

[62] Xu, C.-Y., Hou, B., Wang, Z., Zhang, Y.-T., and Sun, J.-H. “Effect of Mach Number on the Compressible Flow Past a Wavy-Axis Cylinder.” *Aerospace Science and Technology*, 2020, p. 105943.

<https://doi.org/10.1016/j.ast.2020.105943>

[63] Krol, M. C., Molemaker, M. J., and de Arellano, J. V. G. “Effects of Turbulence and Heterogeneous Emissions on Photochemically Active Species in the Convective Boundary Layer.” *Journal of Geophysical Research: Atmospheres*, Vol. 105, No. D5, 2000, pp. 6871–6884.

<https://doi.org/10.1029/1999JD900958>

[64] Duwig, C., Nogenmyr, K.-J., Chan, C., and Dunn, M. J. “Large Eddy Simulations of a Piloted Lean Premix Jet Flame Using Finite-Rate Chemistry.” *Combustion Theory and Modelling*, Vol. 15, No. 4, 2011, pp. 537–568.

<https://doi.org/10.1080/13647830.2010.548531>

[65] Huete, C., Sánchez, A. L., and Williams, F. A. “Diffusion-Flame Ignition by Shock-Wave Impingement on a Hydrogen–Air Supersonic Mixing Layer.” *Journal of Propulsion and Power*, 2016, pp. 256–263.

<https://doi.org/10.2514/1.B36236>

[66] Yamashita, H., Shimada, M., and Takeno, T. A Numerical Study on Flame Stability at the Transition Point of Jet Diffusion Flames. No. 26, 1996, pp. 27–34.

[https://doi.org/10.1016/S0082-0784\(96\)80196-2](https://doi.org/10.1016/S0082-0784(96)80196-2)

[67] Kolla, H., Grout, R. W., Gruber, A., and Chen, J. H. “Mechanisms of Flame Stabilization and Blowout in a Reacting Turbulent Hydrogen Jet in Cross-Flow.” *Combustion and Flame*, Vol. 159, No. 8, 2012, pp. 2755–2766.

<https://doi.org/10.1016/j.combustflame.2012.01.012>

[68] Luo, Z., Yoo, C. S., Richardson, E. S., Chen, J. H., Law, C. K., and Lu, T. “Chemical Explosive Mode Analysis for a Turbulent Lifted Ethylene Jet Flame in Highly-Heated Coflow.” *Combustion and Flame*, Vol. 159, No. 1, 2012, pp. 265–274.

<https://doi.org/10.1016/j.combustflame.2011.05.023>

[69] Boivin, P., Dauplain, A., Jiménez, C., and Cuenot, B. “Simulation of a Supersonic Hydrogen–Air Autoignition-Stabilized Flame Using Reduced Chemistry.” *Combustion and Flame*, Vol. 159, No. 4, 2012, pp. 1779–1790.

<https://doi.org/10.1016/j.combustflame.2011.12.012>

